

Age patterns in a sample of spiral galaxies

M. Carmen Sánchez-Gil¹*, D. Heath Jones², Enrique Pérez¹, Joss Bland-Hawthorn³, Emilio J. Alfaro¹, and John O’Byrne³

¹*Instituto de Astrofísica de Andalucía, Glorieta de la Astronomía s/n, Aptdo. 3004, 18080 Granada, Spain*

²*Australian Astronomical Observatory, PO Box 296, Epping, NSW 2121, Australia*

³*Sydney Institute for Astronomy, School of Physics, University of Sydney, NSW 2006, Australia*

2011 February

ABSTRACT

We present the burst ages for young stellar populations in a sample of six nearby (< 10 Mpc) spiral galaxies using a differential pixel-based analysis of the ionized gas emission. We explore this as an alternative approach for connecting large-scale dynamical mechanisms with star formation processes in disk galaxies, based on burst ages derived from the $H\alpha$ to far UV (FUV) flux ratio. Images of each galaxy in $H\alpha$ were taken with Taurus Tunable Filter (TTF) and matched to FUV imaging from GALEX. The resulting flux ratio provides a robust measure of *relative* age across the disk which we discuss in terms of the large-scale dynamical motions. Systematic effects, such as a variable initial mass function (IMF), non-solar metallicities, variable star-formation history (SFHs), and dust attenuation, have been used to derive estimates of the systematic uncertainty.

The resulting age maps show a wide range of patterns outside of those galaxies with the strongest spiral structure, confirming the idea that star formation is driven one by several processes, largely determined by the individual circumstances of the galaxy. Generally, grand design spirals such as M74, M100, and M51 exhibit age gradients across the main spiral arms, with the youngest star formation regions along the central and inner edges. Likewise, in the dominant star-forming complex of IC 2574 or the ring of M94, the most recent star formation is centrally confined to the regions of star formation activity. In M63 and M74 galaxy-wide trends emerge, suggesting that although most star formation is located along spiral arms, spiral density waves are not the only driver in these cases. We argue that despite appearances, galaxy morphology is not an absolute discriminator of the star formation history of an individual galaxy, nor of the processes triggering it. We conclude that $H\alpha$ -to-FUV flux ratios are a relatively direct way to probe burst ages across galaxies and infer something of their dynamical histories, provided that sources of systematics are properly taken into account.

Key words: galaxies: spiral - galaxies: structure - stars: formation - ISM: HII regions - ISM: general .

1 INTRODUCTION

The origin and persistence of spiral structure in galaxies is still largely an open question, although several plausible alternatives have been hypothesised. In some cases, spiral structure has variously been attributed to tidally influences of companions, a central rotating bar, or orbiting dark matter clumps (e.g. Bottema 2003; Dubinski et al. 2008). Alternatively, spirals density waves may be self-excited, either through quasi-steady global modes of the underlying disk

(Lin & Shu 1964; Bertin & Lin 1996), or as short-lived, recurrent transient patterns from self-gravitational instabilities (Toomre 1964, 1990; Sellwood & Carlberg 1984). Central to all these hypotheses is the need distinguish between transient and ongoing star-formation on the very small scales (< 1 kpc).

Spatial variation in the current star formation rates (SFR) and star formation history (SFH) across a galaxy can provide vital clues to its dynamical and secular evolution. Grebel (2000) finds that galaxy mass and environment are important factors in determining SFH, and finds a diversity of star formation and enrichment histories among

* E-mail: sanchezg@iaa.es

galaxies of the Local Group, even for galaxies with the same morphological type. The most common star formation diagnostics use far ultraviolet (FUV), far-infrared (FIR), or nebular recombination lines (Kennicutt 1998). UV emission is mainly dominated by OB stars, that have lifetimes $\lesssim 10^8$ yr (Iglesias-Páramo et al. 2004, Kennicutt, 1998). In contrast, the H α line is strong only in the presence of the most massive, hot O stars (masses $> 10M_{\odot}$, ages < 20 Myr) with sufficient UV output to ionize the surrounding hydrogen. These stars have even shorter lifetimes ($\lesssim 10^7$ yrs; Iglesias-Páramo et al. 2004; Kennicutt 1998) as they rapidly evolve off the main sequence, making the resulting H α emission the most instantaneous probe of star formation.

The ratio of the UV to H α flux therefore gives a good relative indicator of very recent star formation history (SFH). As a nascent star forming region evolves, the H α line emission declines earlier than the UV continuum, leading to a decrease in the H α /FUV ratio. With appropriate assumptions about the amount of extinction by dust and the nature of the initial mass function (IMF), this ratio is a direct indicator of the age of a new star forming region. Various authors have pointed to other factors that could influence H α /FUV flux ratio, such as variations in the initial mass function (IMF), star formation history (SFH), and metallicity (e.g. Iglesias-Páramo 2004, Meurer et al. 2009, Lee et al. 2009). Different levels of dust attenuation between individual HII regions also has a major influence, especially in the highly extinguished FUV region. Clearly, any effort to use H α /FUV fluxes needs to account for these systematics insofar as the data allow.

Traditional comparisons between star forming distributions have concentrated on identifying entire HII regions as individual, distinct sources. Commonly, workers in the field select HII regions by eye (e.g. Zurita et al. 2001; Battinelli et al. 2000; Rozas et al. 2000; Knapen 1998; Kennicutt 1998). However, such techniques are necessarily subjective and therefore difficult to standardise or reproduce. The flux thresholds at which regions are defined can vary significantly between different observers, and the ability to differentiate individual HII regions from more clumpy structures becomes compromised. Alternatively, region-finding codes, such as *SExtractor* (Bertin & Arnouts, 1996) and *REGION* (developed by C. Heller) search through an image for regions bounded by a chosen flux or luminosity threshold. However, such codes rely on the user subjectively placing the boundaries of HII regions, or manually separating HII regions that are situated too closely to allow easy discrimination by the software. Furthermore, the threshold flux is critically dependent achieving good background subtraction which is notoriously difficult in the field of a nearby galaxy. Clearly by avoiding the need to explicitly define HII regions at all, one removes a major source of systematic error.

To this end, we are motivated to use a pixel-by-pixel differential comparison of star formation regions, analogous to the pixel Colour-Magnitude Diagrams of Lanyon-Foster et al. (2007), and earlier work by Abraham et al. (1999) and Eskridge et al. (2003). This technique provides information on the global SF properties of a galaxy without the need to define HII regions. In principle, such measurements are completely characterised by pixel scale, spatial resolution, and flux threshold, and so are therefore fully reproducible over a diverse sample of galaxies.

In this paper we derive age maps for a sample of six nearby spiral galaxies, using pixel-based methods. Section 2 describes the data and its reduction, including the methodology of the pixel-based mapping technique and corrections for extinction. We also describe our adopted model for the age calibration and explore its dependency on star formation history, metallicity, and initial mass function. In Section 3 we present our age maps and discuss them for each galaxy in turn. In Section 4 we analyse the uncertainties and robustness of this method in the context of both random and systematic error. Section 6 contains a brief discussion and conclusions from this work.

2 SAMPLE AND DATA

2.1 Galaxy Selection

The galaxies in our sample were selected across a range of star-forming types based on their orientation and proximity. Members were chosen to be as face-on as possible to mitigate the effects of extinction and scattering, as well as minimising the wavelength shift in H α due to galactic rotation. Galaxies were also chosen with distances nearer than 10 Mpc to allow sufficient spatial resolution to resolve individual star forming structures within spiral arms. Finally, all galaxies in the sample have archival UV images from the Galaxy Evolution Explorer (GALEX¹, Martin et al 2005) database and far-infrared images from the *Spitzer* Infrared Nearby Galaxies Survey (SINGS², Kennicutt et al 2003). The former are used for age dating and to provide estimates of extinction, while the latter are necessary for dust extinction correction. The final sample consisted of 6 spiral galaxies, ranging from early to late-type. Two of the spirals are barred, M100 and IC 2574, and all have spatially-resolved HI (Martin 1998). A summary of their main properties is presented in Table 1.

Optical images were obtained in H α using the Taurus Tunable Filter (TTF; Bland-Hawthorn & Jones 1997) on the William Herschel Telescope (WHT) on 1999 March 4–6. Conditions were photometric with stable seeing of 1.0 arcsec. TTF was tuned to a bandpass of width $\Delta\lambda = 20$ Å centred at $\lambda_c = 6570$ Å. The intermediate-width R0 blocking filter ($\lambda_c/\Delta\lambda = 6680/210$ Å) was used to remove transmissions from all but a single interference order. Table 2 gives details of the observational set-up. Each galaxy was integrated for 1800 s in H α and either 120 or 300 s in the continuum (Table 3).

The UV images come from the Nearby Galaxies Survey of the Galaxy Evolution Explorer mission (NGS survey, GALEX, Martin et al. 2005). This survey contains well-resolved imaging (1.5 arcsec pix^{-1}) of 296 and 433 nearby galaxies for GR2/GR3 and GR4 releases, respectively, in two passbands: a narrower far-ultraviolet band (FUV; $\lambda_{\text{eff}}/\Delta\lambda = 1516/268$ Å), and a broader near-ultraviolet band (NUV; $\lambda_{\text{eff}} = 2267/732$ Å). Archival *Spitzer* images for the galaxies of the sample were used to provide additional estimates of extinction.

¹ <http://galex.stsci.edu/GR2> and GR4

² <http://sings.stsci.edu/>

Table 1. Galaxy Parameters^a

Galaxy	RA (J2000) h m s	Dec. (J2000) ° ' "	Type	Redshift	Dist. ^b (Mpc)	pc/' ^c	Inclin. ^d (deg)	Dimensions (arcmin)	M _B
NGC 628 (M74)	01 36 41.70	+15 46 59.4	SA(s)c	0.002192	11.4	55.27	5	10.5×9.5	9.95
IC 2574	10 28 21.25	+68 24 43.2	SAB(s)m	0.000190	4.0	19.39	77	13.2×5.4	10.80
NGC 4321 (M100)	12 22 54.90	+15 49 21.0	SAB(s)bc	0.005240	16.1	78.06	30	7.4×6.3	10.05
NGC 4736 (M94)	12 50 53.06	+41 07 13.7	(R)SA(r)ab	0.001027	4.7	22.79	35	11.2×9.1	8.99
NGC 5055 (M63)	13 15 49.25	+42 01 49.3	SA(rs)bc	0.001681	8.4	40.72	55.2	12.6×7.2	9.31
NGC 5194 (M51)	13 29 52.71	+47 11 42.6	SA(s)bc pec	0.00154	8.1	39.27	20	11.2×6.9	8.96

^a Sourced from *NASA Extragalactic Database* : – Position reference – 20032MASX.C, 1991RC3.9C (M51a); – Redshift – Lu *et al.* (1993), Huchtmeier & Skillman(1998), Rand(1995), Mulder & van Driel (1993), 1991RC3.9C, Turner & Ho (1994), respectively for each galaxy.

^b References : (M74) Tully, 1988, Nearby Galaxies Catalogue; (IC 2574) Karachentsev *et al.*, 2002, A&A 383, 125; (M100) Paturel *et al.*, 2002, A&A 389, 19; (M94) Tonry *et al.*, 2001, ApJ 546, 681; (M63) Kennicutt *et al.*, 2003, PASP 115, 928; (M51) Feldmeier, Ciardullo, & Jacoby, 1997, ApJ 479, 231.

^c Scale in pc per arcsec in the final H α images and the age maps plots, where the pixel scale is 1.5''/px.

^d Martin & Kennicutt 2001; Dumke *et al.* 2008; K.T. Chyzy *et al.* 2008.

Table 2. Instrument set-up for H α observations

Date	1999 March 4 – 6
Telescope	WHT
Focal station	f/8
Detector	TEK2
Pixel scale (arcsec/pixel)	0.56
Field of view (arcmin)	15
seeing (arcsec)	1.0
tunable filter	RTTF
H α filter (R0)	$\lambda\lambda$ 668 – 24 nm
H α continuum (R1)	$\lambda\lambda$ 710 – 28.5 nm
H α continuum (R3)	$\lambda\lambda$ 760 – 32.6 nm

Table 3. Log of optical and UV exposures (in seconds)

Galaxy	t _{Hα} ^a	t _{cont} ^b	t _{NUV} ^c	t _{FUV} ^d
NGC628 (M74)	1800	300	1644	1644
IC 2574	1800	120	1861	1861
NGC4321 (M100)	1800	300	2962	1773
NGC4736 (M94)	1800	300	4019	4019
NGC5055 (M63)	1800	120	1660	1660
NGC5194 (M51a)	1800	120	2539	2539

^a H α image exposure time.

^b Continuum image exposure time.

^c GALEX near-ultraviolet (NUV) exposure time.

^d GALEX far-ultraviolet (FUV) exposure time.

2.2 Data Reduction

The optical tunable filter data were reduced using standard IRAF³ tasks, as well as some written specifically for tunable filter data. Bad pixel data were corrected using the IRAF `proto.fixpix` task and the median bias level in the

overscan regions was subtracted from all frames. Both emission line and continuum images from TTF were flat fielded using a combination of dome and sky flats. Continuum images used sky flats for the corresponding broad-band filter. Night sky rings were present in most TTF images due to the well-known phase variation of transmission wavelength with changing off-axis angle. To remove this effect we assumed fixed ring pattern with radial variation centered on the optical axis and fit and subtracted the background azimuthally, as described in Jones *et al.* (2002).

Flux calibration of the continuum-subtracted TTF emission-line images was done following Bland-Hawthorn (1995). The TTF bandpass is sufficiently narrow that fluxes can be converted from counts to physical units (erg cm⁻² s⁻¹ Å⁻¹) by multiplying the total counts per second by the CCD gain, and dividing by the reduced telescope area, (which takes the central Cassegrain obstruction into account). This was then divided by the total system efficiency (telescope plus instrument), determined from published spectrophotometric standard star fluxes (Oke 1990). Standard stars were observed during each observing run at the same TTF plate spacings as for the science frames.

We first resampled and aligned our H α , UV, and FIR image data onto a common pixel scale and orientation. Images were trimmed to a common field size, rotated to north-up east-left, and resampled to the lowest scale of all frames (1.5 arcsec pix⁻¹), using the IRAF tasks `magnify`, `geomap`, and `geotran`. This pixel scale is an intermediate value between the better of H α (0.56'') and the worst (4.5 and 9''). 1.5'' is the scale of FUV and 24 μ m images. It is truth that the actual scale of the resulting TIR image should be 9'', or a bit smaller, but not 1.5''. We could be overestimating the flux. But when we resample using 3×3 and 6×6 binnings, resulting scales of 4.5'' and 9'' respectively, we check that the age structures and gradients remain the same (described in Section 4.2). Individual FIR frames were combined into a single total infrared image as described above. The effects of binning the data in this way were investigated and are discussed in Section 4.2. Galaxy fields were masked to a common area across the H α , UV and combined FIR frames. Those galax-

³ IRAF is the *Image Reduction and Analysis Facility*, produced by the National Optical Astronomy Observatories (NOAO).

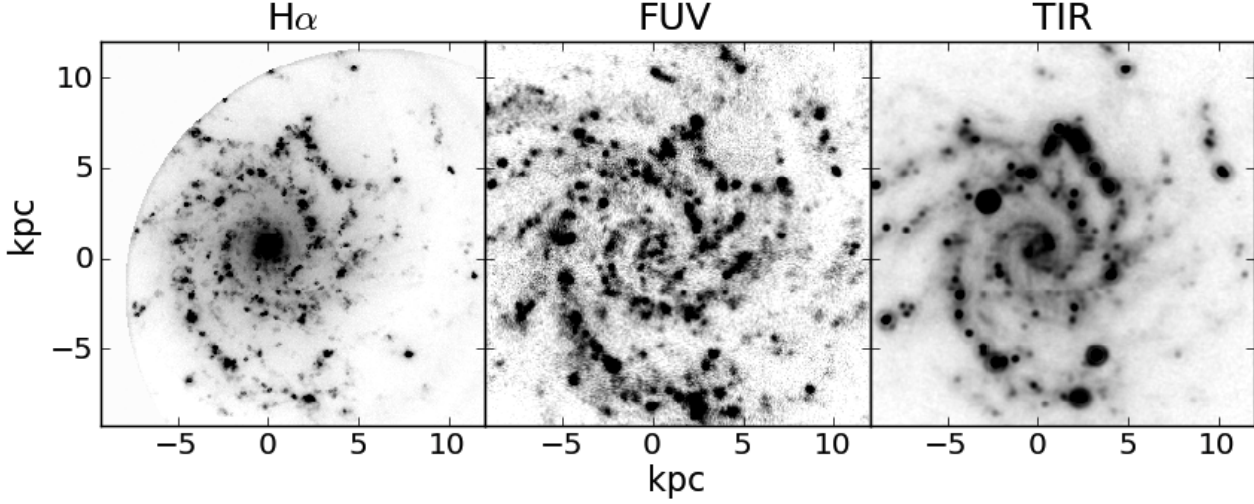


Figure 1. Examples of processed frames in $H\alpha$ (left), far ultraviolet (FUV; centre), and total infrared (TIR; right) for the galaxy M74. The images have been resampled to have identical size, orientation, and pixel scale ($1.5''/\text{pix}$).

ies with prominent bulges (M51 and M74) also had these central regions removed, as were foreground Galactic stars and CCD artifacts.

Galactic extinction was corrected using the Schlegel et al. (1998)⁴ dust maps for colour excess $E(B - V)$. The extinction, A_λ , at wavelength λ was determined from

$$A_\lambda = k_\lambda E(B - V) \quad (1)$$

where $k_{H\alpha} = 2.54$, $k_{FUV} = 8.22$ and $k_{NUV} = 8.20$ using a Cardelli et al. (1989) extinction curve and $R_V = 3.1$.

Internal extinction for the galaxies in our sample was calculated in a two stages. First, the *Spitzer* images at 24, 70, and 160 μm for each galaxy were combined into an image of total far-infrared (TIR) flux, according to

$$F_{TIR} = \zeta_1 \nu F_\nu(24\mu\text{m}) + \zeta_2 \nu F_\nu(70\mu\text{m}) + \zeta_3 \nu F_\nu(160\mu\text{m}) \quad (2)$$

where $[\zeta_1, \zeta_2, \zeta_3] = [1.559, 0.7686, 1.347]$, (Dale & Helou 2002). The different plate scales for each frame ($1.5 \text{ arcsec pix}^{-1}$ for 24 μm , $4.5 \text{ arcsec pix}^{-1}$ for 70 μm , and $9 \text{ arcsec pix}^{-1}$ for 160 μm) were all resampled to $1.5 \text{ arcsec pix}^{-1}$ where necessary, identical to that of the optical and GALEX (FUV and NUV) frames. With this in hand, a value for the FUV extinction, A_{FUV} , was then derived through Eqn. 2 of Buat et al (2005),

$$A_{FUV} = -0.0333y^3 + 0.3522y^2 + 1.1960y + 0.4967, \quad (3)$$

which relates the TIR-to-FUV flux ratio, $y = \log(F_{TIR}/F_{FUV})$, also referred to as the infrared-excess (IRX). This expression, and the TIR-to-FUV flux ratio, appear to be much a more robust and universal tracer of dust extinction than other methods. As a quantitative dust estimator, it is found to be almost independent of dust and stellar geometry, provided that the galaxies are forming stars actively (Buat & Xu 1996; Buat et al. 1999; Gordon et al. 2000). With no available $H\beta$ data, the $A(H\alpha)$ extinction

was calculated using the relation $A_{FUV} = 1.4A(H\alpha)$ of Boissier et al. (2005).

2.3 Age calibration

Model $H\alpha$ and FUV luminosities were generated from Starburst99 (Leitherer et al. 1999; Vázquez & Leitherer 2005). The code can be run with two different star formation modes: an instantaneous burst or continuous. In choosing our model inputs we considered three alternatives in the stellar initial mass function, (IMF):

- (i) Case A: a Salpeter law with $\alpha = 2.35$ and $M_{up} = 100M_\odot$ (our reference model),
- (ii) Case B: a truncated Salpeter law with $\alpha = 2.35$ and $M_{up} = 30M_\odot$, and
- (iii) Case C: a Miller-Scalo law with $\alpha = 3.3$ and $M_{up} = 100M_\odot$,

Five metallicities were used for each IMF: $Z = 0.04$, 0.02 (solar, Z_\odot), 0.008 , 0.004 and 0.001 .

The full models cover the age range 10^6 to 10^9 yr in steps of 1 Myr with spectral energy distributions (SEDs) spanning 100 \AA to $1 \mu\text{m}$ in wavelength. However, we restricted the ages from 1 to 10 Myr as we are only interested in the youngest stellar populations responsible for the $H\alpha$ and UV output. We compute our model luminosities as

$$\log(L_{H\alpha}) = \log(EW(H\alpha)) + \log(C(H\alpha)) \quad (4)$$

$$L_{FUV} = \frac{\int F(\lambda)S(\lambda)d\lambda}{\int F(\lambda)d\lambda} = \frac{\sum_{\lambda=1341}^{1809} F(\lambda)S(\lambda)}{\sum_{\lambda=1341}^{1809} F(\lambda)} \quad (5)$$

where $EW(H\alpha)$ is the $H\alpha$ equivalent width (in \AA), and $C(H\alpha)$ is the $H\alpha$ continuum (measured as the median continuum luminosities at wavelengths 6550 and 6590 \AA). The $F(\lambda)$ term in Eqn. 5 is the GALEX response curve and $S(\lambda)$ is the luminosity of the SED in units of $\text{erg s}^{-1} \text{\AA}^{-1}$.

⁴ <http://www.astro.princeton.edu/~schlegel/dust/data/data.html>

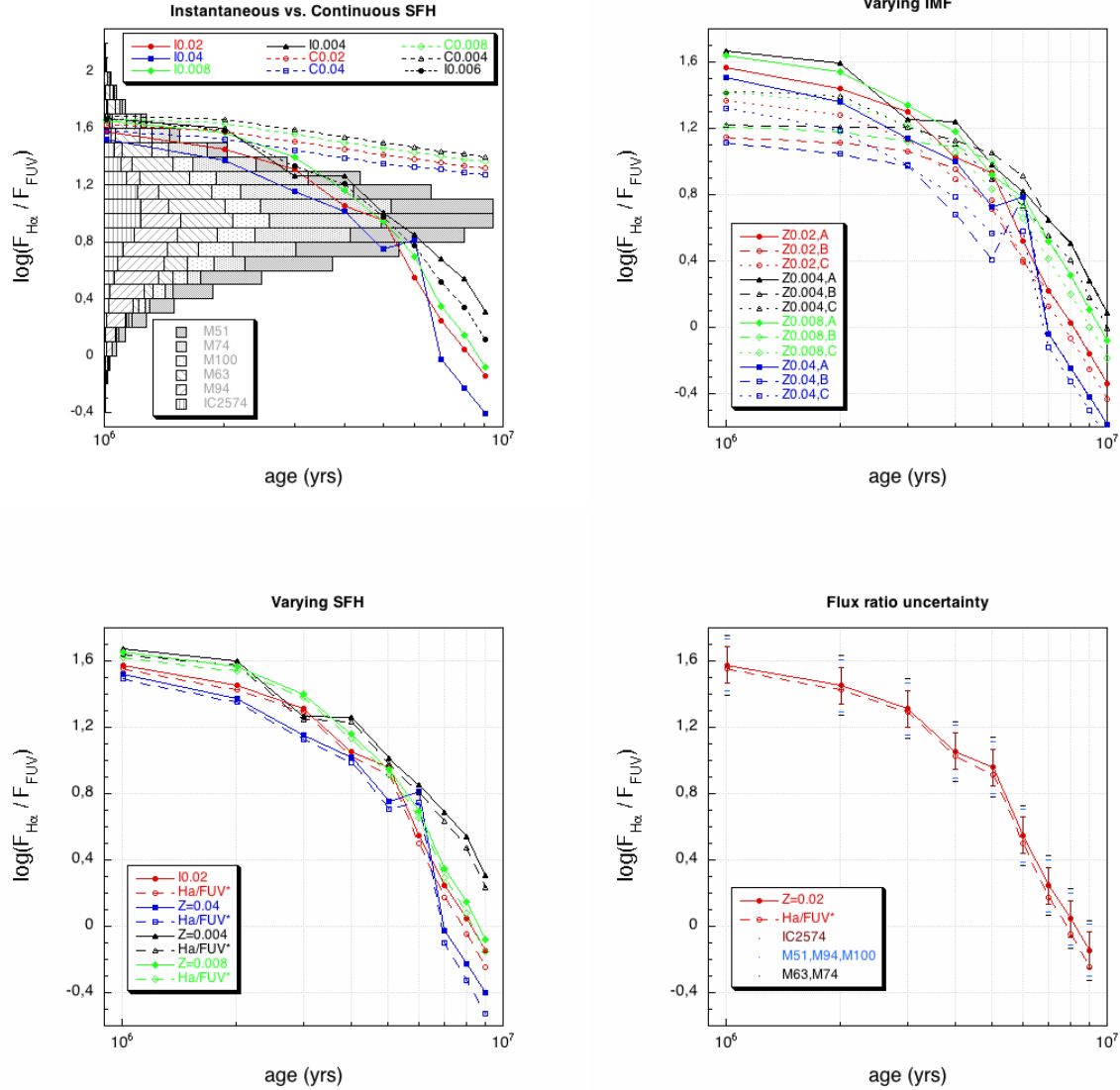


Figure 2. The effect of varying SFH, IMF, and metallicity on model $H\alpha$ to FUV flux ratios, $\log(F_{H\alpha}/F_{FUV})$. *Upper left:* Flux ratio in the case of both instantaneous (dashed lines) and continuous SFHs (solid lines). The models in this panel assume a Salpeter IMF and range of metallicities: $Z = 0.02$ (red circles), 0.04 (blue squares), 0.008 (green diamonds) and 0.004 (black triangles). The underlying histogram shows the range of measured flux ratios for each galaxy in the sample. *Upper right:* Model $H\alpha$ to FUV flux ratios as a function of varying IMF: (A) Salpeter, $\alpha = 2.35$ and $M_{up} = 100M_{\odot}$; (B) truncated Salpeter, $\alpha = 2.35$ and $M_{up} = 30M_{\odot}$; (C) and Miller-Scalo, $\alpha = 3.3$ and $M_{up} = 100M_{\odot}$. In these cases, the assumed SF law is instantaneous and the metallicities are the same as those in the *upper left* panel, and with the same colour coding. *Bottom left:* A comparison between an instantaneous SFH with recent 25 Myr-old burst (dashed lines) to a plain instantaneous burst (solid lines). The latter are the same solid curves as shown in the *upper left* and the same metallicities (and their colours) have been used. *Bottom right:* A comparison of the systematic model uncertainties with random uncertainty in the flux measurements. The instantaneous and (instantaneous+recent burst) models are shown (solid and dashed red lines, respectively). Photometric measurement errors for the galaxies (in three groups) are indicated by the horizontal bars.

To assess the suitability and robustness of our reference model we calculated the effect of changing various model inputs on the SB99 $F_{H\alpha}/F_{FUV}$ ratios (Figure 2). The upper left panel shows of Fig. 2 shows the ratios for both an instantaneous and continuous SFH, and shows the former to be much better match to the observed ratios. Like Iglesias-Páramo *et al.* (2004), we find an instantaneous SFH to be a

more sensitive discriminant of the age variations in younger star forming regions. One might naively assume that because our galaxies are not starbursts they would be better modeled assuming continuous star formation. However, as our pixel approach delineates individual star forming regions (as opposed to integrating the total star formation across the face of the galaxy), each particular star-forming region, repre-

sented by a pixel in the image, is more accurately regarded as having undergone a stellar burst. Although the SFHs of individual regions will be more complex, an instantaneous starburst is a reasonable approximation for localised regions of star formation younger than 10^8 yr (e.g., Pasquali et al. 2008).

In the upper right panel of Fig. 2 we show the effect that changing the IMF has on the $H\alpha$ -to-UV ratio for a range of metallicities. All three cases of IMF are shown (A, B, and C) which represent a plausible spread of slopes and mass cut-offs. For each case we apply metallicities of $Z = 0.02$ (solar), 0.04, 0.004, and 0.008. We see that for fixed metallicity, the variation between the different IMFs is no more than 0.4 dex for the youngest ages, reducing to ~ 0.1 dex beyond ~ 6 Myr. Alternatively, for a given fixed IMF, the variation in $H\alpha$ -to-UV with metallicity is at most ~ 0.5 dex over the longest ages, reducing to ~ 0.2 dex within the first few Myr.

We would expect that the $H\alpha$ -to-UV ratios are especially sensitive to SFHs that containing a recent burst of star formation (say 25 Myr). These would no longer emit in $H\alpha$ but still carry some output in the FUV given the relatively longer ages of the lower mass UV-emitting stars. To investigate this, we compute F_{UV}^* which is the FUV flux generated from a current burst of star formation combined with a 25 Myr-old burst with identical SFR. In the lower left panel of Fig. 2 we compare the flux ratio $F_{H\alpha}/F_{FUV}^*$ (for a SFH with an additional burst) to the same ratios $F_{H\alpha}/F_{FUV}$ plotted in the upper left (for an instantaneous SFH). The figure shows that there is negligible difference (< 0.15 dex) between either case of SFH, for a fixed given metallicity. We therefore conclude that recent bursts are much less of an effect on the FUV than one might expect.

The lower right panel of Fig. 2 puts the size of this variation due to SFH into the context of the measurement errors. The red solid and dashed lines show the reference model for both the instantaneous and (instantaneous+ recent burst) cases. Also shown at each point are the 1σ measurement uncertainties for all of the galaxies. We see that compared to the observational errors, systematic uncertainty due to the SFH is negligibly small.

We conclude that of all the model inputs, it is choice of IMF that matters most over the first few Myr after an instantaneous burst of star formation. Metallicity matters more after several Myr have elapsed, and in both cases the range is 0.4 to 0.5 dex at most, and is comparable with the observation errors. We also conclude that a continuous SFH can be ruled out on the basis of our observed $F_{H\alpha}/F_{FUV}$ ratios, and that an instantaneous burst gives a more realistic distribution of values. While one might expect that the addition of a recent burst of (25 Myr ago) would affect the FUV flux significantly, we find that this is not the case. Most important of all, we see that while the change in $H\alpha$ -to-UV fluxes in *absolute* terms is about 0.4 to 0.5 dex due to changing model inputs, the change in *relative* terms (i.e. difference from 1 to 10 Myr) is much less (< 0.15 dex). Therefore, any relative age comparisons are largely immune to the choice of model inputs.

3 AGE MAPS

Once the alignment and re-scaling of the images is done, we are in a position to derive calibrated age maps for the sample. We adopt our reference model which assumes an instantaneous star formation law and Salpeter IMF ($\alpha = 2.35$, $M_{up} = 100M_{\odot}$). In each case we assume solar metallicity, except for IC 2574 where an interpolation between $Z = 0.004$ and $Z = 0.008$ is applied. Radial oxygen abundances from Pilyugin et al. (2004) for all galaxies indicate that solar metallicity is representative of their mean abundances. In the case of IC 2574, Miller & Hodge (1996) give $12+\log(O/H) \sim 8.15$, $\sim 30\%$ and a solar metallicity 8.69, which is why we have adopted the interpolated value $Z = 0.006$ for this object. The flux ratio is calibrated into SB99 model ages at ten intervals of 1 Myr, starting at 1 Myr. This age resolution is dictated by the internal precision of the flux ratio.

Figure 3 shows the age maps for all galaxies. Each pixel in the map is assigned a range rather than a single valued age, which is comparable to the photometric flux uncertainties and improves clarity. The maps are contoured in three or four age bins from the set 0 – 4 Myr, 4 – 6 Myr, 6 – 9 Myr and older than 9 Myr. We discuss each galaxy in turn.

3.1 M74 (NGC 628)

M74 is a well-studied late-type SA(s)c spiral at a distance of around 11.4 Mpc (Table 1) with a pair of tight spiral arms (< 15 kpc) and no obvious bulge. Deep $H\alpha$ imaging has revealed numerous HII regions in two outer arms at 17 kpc (Lelièvre & Roy 2000). Cornett et al (1994) found the star formation history of this galaxy to vary with radius, consistent with the observation by Natali et al (1992) that M74 contains an inner stellar population (< 1.5 Holmberg radii = $9' = 10$ kpc) distinct from the outer disc. This separate nature of the inner disc is supported by kinematic data (Fathi et al 2007) and Lick indices from the centermost region (Ganda et al 2007).

Figure 3 shows our age map for M74. The nucleus of the galaxy is small and bright and was saturated in our $H\alpha$ maps, and so was masked. The age map shows an age gradient from the inner to the outer parts of the galaxy, from very recent to less recent episodes of star formation, in agreement with previous authors (Cornett et al. 1994, Lelièvre & Roy 2000). Specifically, we find that the $H\alpha$ luminosity decrease in radius is more pronounced in the inner 5 to 6 kpc, while the UV luminosity shows a shallower rate of change. Consequently, the $H\alpha$ /FUV ratio decreases with radius indicating an age increases in the outward direction (Fig. 3). Cepa & Beckman (1990) locate the corotation radius at ~ 6 kpc, although this distance is too close to the outer limit of our data to allow any conclusions about the effect of corotation to be drawn (see also our discussion of M51 below).

On more localised scales, the short arm that opens S-SW at 4 kpc shows a clear age gradient across it. The outer longer arm, that runs SE-S at ~ 5 to 10 kpc, shows a less marked age gradient across its width. If the age gradients across spiral arms are a direct product of the spiral density wave, then the dilution of the gradient in this southern arm may be related to the weakness of the density wave or the approach to corotation. As discussed by Efremov (2009),

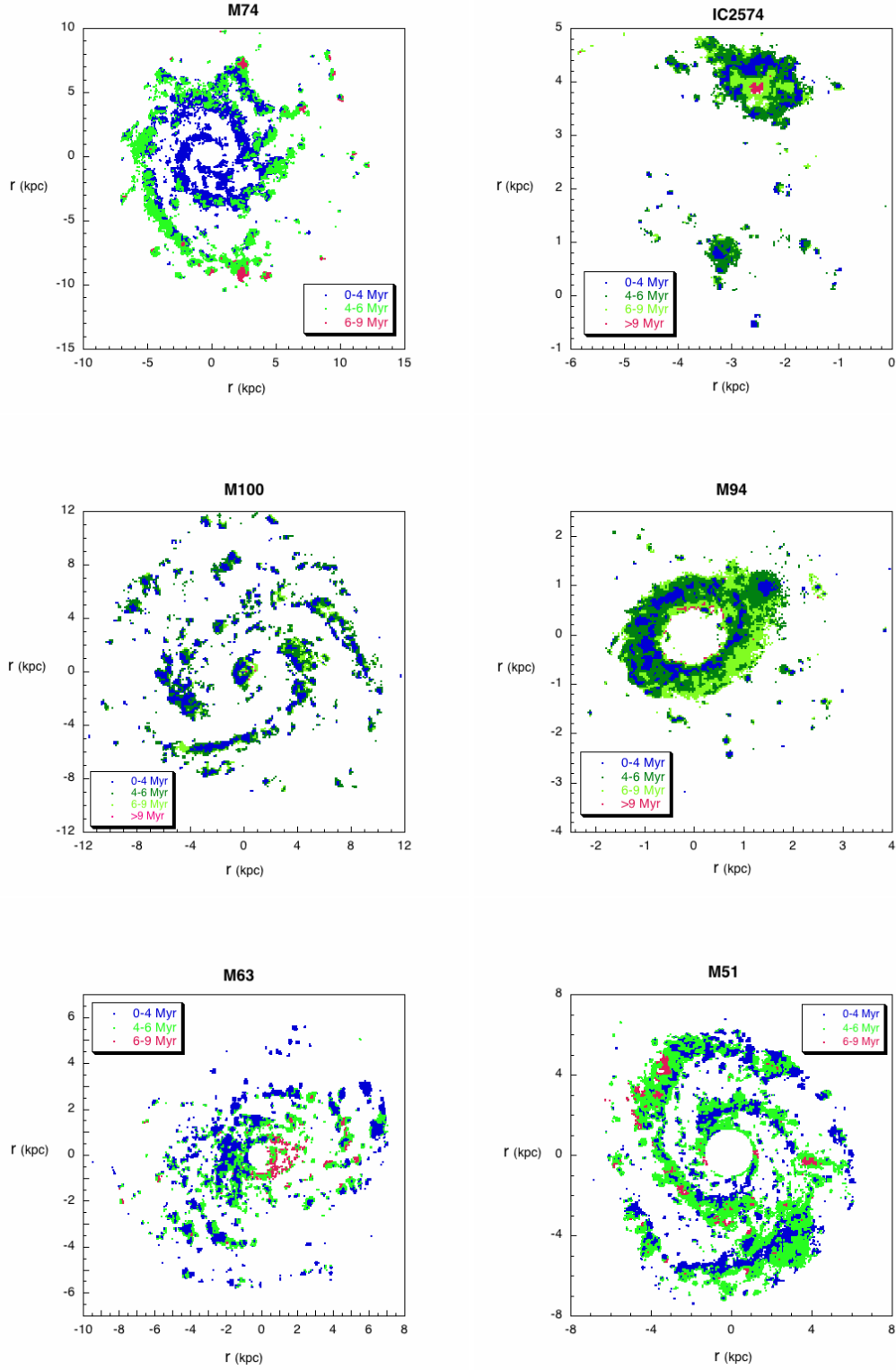


Figure 3. Age maps for the galaxies of our sample using the default model, with age denoted by colour as indicated in the key. Note that different colour schemes apply to those galaxies with only three age bins (M74, M63, and M51) and the remaining galaxies with four. The axes are in kpc and centred on each galaxy. North is up, east to the left.

the presence of a shock produced by the spiral density wave, (made visible by dust lanes along the spiral arms), is incompatible with the creation of star forming complexes, because of the absence of visible dust lanes in this arm, despite a chain of complexes along its length. The thickness of the longer arm is basically dominated by a single age range, and the youngest population located in the inner edge of the arm maps the location of the chain of complexes observed in this arm.

An alternative method to gauge the impact of spiral density waves is to check the presence and distribution of an old stellar population in the far infrared. Fig. 4 is an colour composite of M74 in $3.6\ \mu\text{m}$ (blue), $8.0\ \mu\text{m}$ (green) and $24\ \mu\text{m}$ (red) data from the SINGS survey⁵ (Kennicutt et al 2003). The $24\ \mu\text{m}$ image maps the hot dust emission, whereas the $3.6\ \mu\text{m}$ image shows the old stellar population. This shows how the nucleus, the circumnuclear region, and the inner spiral arms of M74 are all dominated by an old population. Cid Fernandes et al. (2004, 2005) and González Delgado et al. (2004) find the majority of the nuclear SED of M74 to be dominated by stars older than 1 Gyr. As is expected for a spiral density wave, the old stellar populations are distributed along the inner spiral arms. In contrast, the same $3.6\ \mu\text{m}$ light is not seen along the outer longer southern arm, instead being dominated by the hot dust of star complexes. Without the influence of a spiral density wave, as outer arm evolves the stars disperse and as a result, the old stellar population is not uniformly distributed along the arm.

A circumnuclear ring of star formation (Wakker & Adler 1995, James & Seigar 1999) prompted speculation of a dust-enshrouded bar. Near-infrared imaging reveals an oval-shaped central distortion, that could be responsible for the circumnuclear ring, (Seigar 2002) and a weak bar, if any. These features are also seen in Fig. 4, and although the nuclear region is masked, the inner regions in the vicinity are within in the youngest age range, < 4 Myr.

3.2 IC 2574

IC 2574 is a gas-rich dwarf galaxy and a member of the M81 group of galaxies. It is classified as SAB(s)m given its HI structure showing two weak spiral arms. In contrast, its H α and UV images show an irregular patchy pattern, which instead suggests a dwarf irregular classification (Weisz et al. 2009; Cannon et al. 2005; Walter & Brinks 1999; Walter et al. 1998). IC 2574 contains numerous HI expanding shells and holes in its interstellar medium. Walter & Brinks (1999) found 45 large expanding shell-like structures in neutral hydrogen, thought to be the combined result of supernova explosions and stellar winds produced by young stellar associations.

Our age map for IC 2574 (Fig. 3) is dominated by the giant (> 1 kpc) H α complex NW of the galactic centre. This complex is associated with a peak in the HI emission (Martimbeau et al. 1994), and with one of the prominent expanding supergiant HI shells (Walter et al. 1998; Walter & Brinks 1999; Weisz et al. 2009). Weisz et al. (2009) found evidence that stellar feedback created the supergiant HI shell with a

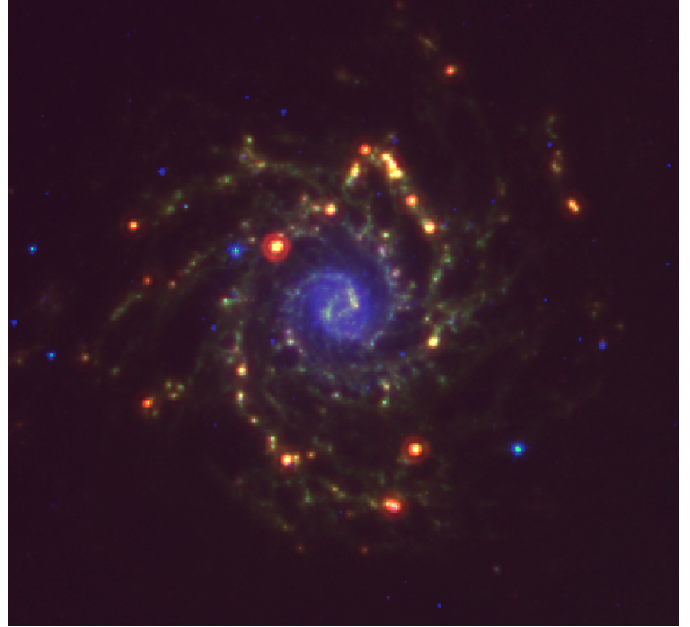


Figure 4. False colour composite of M74 in the far infrared, using $3.6\ \mu\text{m}$ (blue), $8.0\ \mu\text{m}$ (green) and $24\ \mu\text{m}$ (red) data.

recent SF episode interior to the shell, which peaked ~ 25 Myr ago, and triggered secondary star formation (< 10 Myr old) around its rim. This corresponds well to the structures seen in our age map of IC 2574 in Fig. 3. As is typical for giant star forming complexes outside of obvious spiral arms, we find that a younger star forming population surrounds an older one located at the centre. Current star formation, as traced by H α and mid-IR emission, is found along the rims of the larger HI holes, indicative of a propagating pattern of star formation as found by other authors (Walter et al. 1998, Walter & Brinks 1999, Cannon et al. 2005, Martimbeau et al. 1994). Sánchez Gil et al. (2009) find a similar giant star forming complex in NGC 6946 (~ 700 pc in diameter), where a central star formation event (a young and massive super star cluster) initiated the expansion of the shell, which swept up the gas and triggered secondary star formation at the rim of the shell.

3.3 M100 (NGC 4321)

M100 (NGC 4321) is a nearly face-on barred spiral in the Virgo Cluster, (16.1 Mpc distant). The gas kinematics for this galaxy show an intriguing double bar in the gas kinematics, and García-Burillo et al. (1998) use hydrodynamical cloud simulations to fit a two-bar model simultaneously to visible, infrared, HI and CO data. The two independent systems consist of (i) a nuclear bar (with fast pattern speed of $\Omega_f = 160\ \text{km s}^{-1}\text{kpc}^{-1}$ and corotation radius $R_{COR}^F = 1.2$ kpc), decoupled from (ii) an outer bar+spiral with slower pattern speed, ($\Omega_f = 23\ \text{km s}^{-1}\text{kpc}^{-1}$, $R_{COR}^S = 8 - 9$ kpc).

Our age map for M100 shows an azimuthal gradient for ages less than 10 Myr (Fig. 3). The UV image has many bright and extended regions, indicating intense star-formation activity, as a majority of the stars have ages younger than 6 Myr. The edge of the age map falls short of the outer corotation radius, which is not seen in our data.

⁵ <http://sings.stsci.edu/>

The corotation of the fast pattern falls within the inner Lindblad resonance (ILR) of the slow pattern, allowing an efficient transfer of molecular gas towards the nuclear region. Both the increased mass inflow rate and the overall higher gas density in the nuclear ring should be related to the age gradient detected in the circumnuclear ring of M100 (Ryder et al. 2001, Allard et al. 2006, Mazzuca et al. 2008). Allard et al. (2006) find a bipolar azimuthal age gradient from 10 Myr to 50 Myr using the equivalent width of $H\beta$ emission and Ryder et al. (2001) find an azimuthal age distribution 8 to 10 Myr using $Br\gamma$ and CO from IR spectroscopy. This consistent picture of the age gradients found through different diagnostics (sensitive to different age ranges) indicates that the circumnuclear region of M100 has experienced ongoing star formation for at least the past 50 Myr.

The bulk of the circumnuclear star formation events in M100 are best described by starburst models, with decay time-scales of ~ 1 Myr (Ryder, Knapen & Takamiya 2001), as we have used here.

3.4 M94 (NGC 4736)

M94 is an early-type, nearby (4.7 Mpc), spiral with a bright inner region composed of a bright circular bulge surrounded by a ring of active star-forming regions, about 1 kpc from the center (Wong & Blitz 2000). This ring is the dominant feature in the age map of M94 (Fig. 3) and most star formation in the galaxy is circumscribed by this region of young hot stars. Figure 3 shows that the most recent star formation is innermost around the N sector of the star forming ring but moves closer to the inside edge around its S sector. The age map also shows an additional star forming complex on the outer NW edge of the ring. In the UV image a dim bulge and short spiral arms are visible, with the bright ring around the center of the galaxy. In the $H\alpha$ image, the spiral arms were too faint to be seen and the bulge was saturated and so was masked out.

A clear age gradient is observed across the ring, with the younger stars in the middle, surrounded by older ones both in the inner and outer rims. This young burst of star formation in the ring is also seen in Fig. 3 of Trujillo et al. (2009): the color luminosity profiles presented by these authors clearly show that the continuum is enhanced locally at the distance of the ring ($\sim 47''$) in the ultraviolet and blue bands, but not in the redder bands. Furthermore, the PAH emission bands (5.8, 8.0 and 24μ) are locally enhanced in the mid-infrared (MIR) luminosity profiles, but not the NIR or redder FIR bands corresponding to the older stars or colder dust. A cursory glance at the MIR Spitzer spectra indeed show the presence of strong PAH emission (see also Fig. 6 of Trujillo et al. 2009).

The star formation rate computed in the inner part of M94 is $\sim 0.1 M_{\odot} \text{ yr}^{-1} \text{ kpc}^{-2}$, and can be deduced from the data in Boissier et al. (2007, their Fig. 9.39, for $\text{HI} + \text{H}_2$) and Trujillo et al (2009, for their 'bulge' inner region, from FUV data). From our $H\alpha$ image the distribution of pixel-wise SFR is $0.1 M_{\odot} \text{ yr}^{-1} \text{ kpc}^{-2}$ for pixels in the 85 percentile band. Wong & Blitz (2000) analyse CO, HI, and $H\alpha$ data for this ringed galaxy, and conclude that the star formation rate is not determined solely by available gas mass, but rather that large-scale dynamics play a significant role in organizing and possibly triggering star formation.

M94 is not completely axisymmetric but has a large-scale, broad oval that may affect its internal dynamics (Kormendy & Kennicutt 2004). HI synthesis observations (Bosma, van der Hulst, & Sullivan 1977) and optical and near-infrared imaging (Möllenhoff, Matthias, & Gerhard 1995) have demonstrated that the disk of the galaxy is nonaxisymmetric, and hence the rings may occur at the inner and outer Lindblad resonances (ILR and OLR) of an oval potential (Gerin, Casoli, & Combes 1991). Mulder & Combes (1996) found that the potential of M94 can be modeled well with an oval component at intermediate radii. These hydrodynamic simulations suggested that the rotating oval is indeed responsible for the 'rings' formation, revealing the formation of two rings, at 1.5 and 10 kpc radius, which correspond to the ILR and the OLR, with a pattern speed of $40 \text{ km s}^{-1} \text{ kpc}^{-1}$. In addition, Möllenhoff, Matthias, & Gerhard (1995) have suggested that the inner ring may coincide with the OLR of a central stellar bar, $\sim 30''$ in extent, seen in optical and near-infrared isophotes. The rotation curve is consistent with a scenario in which the ring corresponds to the OLR of the nuclear bar and the ILR of the large-scale oval distortion. Such a coupling of nested bars may contribute to the accumulation of gas in the ring (Wong & Blitz 2000). Chyży & Buta (2008) have demonstrated that M94 has highly symmetric and strong magnetic spiral fields, not clearly associated with the shape of the distribution of star-forming regions or with spiral density waves.

3.5 M63 (NGC 5055)

M63 is a nearby, spiral galaxy and one of the prototype arm-class 3 flocculent galaxies (Elmegreen & Elmegreen 1987). It shows a regular, two-arm spiral structure to a radius of 4 kpc in the near-infrared (Luo et al. 2007) and has been studied extensively across the electromagnetic spectrum. Luo et al. (2007) studied the *Chandra* properties of low-and-high mass x-ray binary populations, and concluded that the disk has undergone recent, strong starbursts that significantly increased the population of high-mass x-ray binaries (HMXB). The galaxy has a flocculent appearance in $H\alpha$ and is significantly brighter on the E side than the W. Ongoing starbursts are also observed in the LINER nucleus of M63, which is UV-bright and surrounded by luminous young star clusters, showing clear stellar absorption signatures (Maoz et al. 1998; Leitherer et al. 2002). In our $H\alpha$ data the nucleus is saturated and was masked.

The age map for M63 in Fig. 3 shows an E-W age gradient running across the face of the galaxy. This gives it a peculiar bipolar age distribution, in which the pixels in the older age bin (6 – 9 Myr) are mostly located in the W half of the galaxy, the pixels in the intermediate age bin (4-6 Myr) are more evenly distributed throughout, and the pixels corresponding to the youngest age bin are concentrated towards the east. Within the inner ± 3 kpc, the W side is dominated by an older population (6 – 9 Myr) while the E side is dominated by one younger than 4 Myr.

M63 has been studied in ^{12}CO ($J=1-0$) by Tosaki et al. (2003) and in HI by Battaglia et al. (2006). These authors note the regularity and symmetry of the galaxy, but a mild lopsidedness is noticeable, both in the distribution and the kinematics of the gas. These results point at two different dynamical regimes: an inner region dominated by the stellar

disk and an outer one, dominated by a dark matter halo offset with respect to the disk. They suggest that cloud formation and the ensuing star formation occur both in the arm and the interarm regions due to enhancement of gas by local fluctuations, since no clear systematic offset between the molecular gas and HII regions is found, as neither are Giant Molecular Associations.

The inner < 3 kpc in M63 is conspicuously similar in its spatial structure to the dust distribution and to the velocity field. We have investigated several possible astrophysical causes for an asymmetric age distribution at larger radii. We do not find any possible mechanism that would relate the age map to the velocity field. We have also looked for a possible relation with the extinction correction, based on the appearance of the dust distribution in Fig. 12 of La Vigne et al. (2006). We correct for extinction by means of the FUV/TIR ratio. When this is plotted against the three age bins that span the age range under consideration, the difference of median value of this ratio is only 0.1 between the first and third age bins. This small difference translates to a negligible age increment, and thus the extinction pattern can be rejected as the source for the peculiar age pattern. In the third place we have looked into the polarization pattern as shown in Fig. 3 of Knapik et al. (2000). The polarization vectors are very uniformly distributed in the region where we find the age pattern, so this does not seem to be related either. We have also looked into the relationship with the molecular distribution, as presented by Thornley & Mundy (1997), but the CO distribution is fairly symmetrical both sides of the bulge at ± 2 kpc, so it does not provide any further information. Thornley & Mundy (1997) present a K image in their Fig. 3; and in this image there is a hint of the W side in the inner 2 kpc being brighter than the E side, what is consistent with the age difference we find in the age map of M63.

3.6 M51 (NGC 5194)

M51 is grand-design spiral galaxy interacting with the nearby NGC 5195 and a member of the same group as M63. It is a metal-rich galaxy, $12 + \log(\text{O}/\text{H}) \sim 8.7 - 8.9$ (Bresolin et al. 2004), with a weak metallicity gradient as a function of galactocentric distance (Zaritsky, Kennicutt, & Huchra 1994). Because of its large apparent size and luminosity it is possible to observe a wealth of detail in its arms and spiral structure.

The age map for M51 in Fig. 3 is dominated by a young population of stars (< 6 Myr). It shows an age structure with gradients across the arms, with the younger stars towards the inner edge while the stars in the older age bin are located towards the outer edges. This age pattern is expected if star formation is triggered by gas shocked by the pass of a spiral density wave (Roberts 1969; Martínez-García et al. 2009). If this is the case, we should observe the inverse age pattern outside co-rotation — that is, the youngest population preferentially located radially in the outer side of the arms. Determinations of the co-rotation radius for M51 are in the range $126'' - 161''$ (Vogel et al. 1993; Elmegreen et al. 1992; Knapen et al. 1992; García-Burillo et al. 1993). These estimates correspond to a distance of $\sim 4.9 - 6.3$ kpc; unfortunately our data falls just short of this range, so we are not

able with this data set to confirm whether the age pattern switches at co-rotation.

Calzetti et al. (2005) present a panchromatic view, UV to FIR, of the star formation in M51 and the impact of dust extinction. In their Fig. 1 (left) they present an $(R, G, B) = (24\mu\text{m}, \text{H}\alpha, \text{FUV})$ image that further supports the age pattern across the arms that we find here. What the image shows is the same age pattern with the dust+H α +FUV located towards the inside of the arms, while the outside is dominated by the FUV alone. As we have argued above, Calzetti et al. also state that the UV emission traces predominantly the evolved, non-ionizing stellar population, up to ages $\sim 50 - 100$ Myr. Thus the age pattern that we already see for the ongoing star formation, < 10 Myr, can be extended up to the recent past non-ionizing star formation, that follow in the outer part of the arms. What we are witnessing here is a clear age pattern along the spurs in the arms of the galaxy.

Scheepmaker et al. (2009) have studied the age distribution of 1580 resolved star clusters in M51 from HST UBVI photometry, and their spatial relation to the H α and 20 cm radio-continuum emission. The positions of the youngest (< 10 Myr) clusters show the strongest correlation with the spiral arms, H α , and the 20 cm emission, and these correlations decrease with age (their Figs. 16 and 17). The azimuthal distribution of clusters in terms of the kinematic age away from the spiral arms indicates that the majority of the clusters formed 5–20 Myr before their parental gas cloud reached the centre of the spiral arm. The authors divide the sample in three age ranges, $\log(\text{age}) < 7.0, 7.0 - 7.5, > 7.5$, and find (their Fig. 13) that the oldest clusters have older kinematic ages (10–15 Myr) compared to the intermediate age and to the youngest clusters.

4 RELIABILITY AND ROBUSTNESS

The photometric uncertainty on the $F_{\text{H}\alpha}/F_{\text{FUV}}$ flux ratio is dominated by the error on the FUV flux (15 to 25%) and not H α ($< 5\%$). An additional error term comes from the use of Equation 3 for the FUV extinction correction, which depends on the uncertainties in the FIR. The uncertainties for the $24\mu\text{m}$, $70\mu\text{m}$ and $160\mu\text{m}$ fluxes are 4%, 7% and 12% respectively (Dale et al. 2007), implying 6% uncertainty overall in F_{TIR} and 13% in the $F_{\text{TIR}}/F_{\text{FUV}}$ ratio. With the application of the extinction correction the overall uncertainty in the $F_{\text{H}\alpha}/F_{\text{FUV}}$ flux ratio is more like 28%.

Photometric uncertainties aside, the age-dating technique is subject to a number of potential sources of systematic error. In this section we test the robustness of our results to systematics by varying the assumptions we have made over a plausible range of values. Specifically, the effects we examine are (i) the lowest limit on cluster mass allowable for our assumptions on ionizing flux, (ii) the effect of changing the spatial bin size, and (iii) the effect of changes to the metallicity and IMF assumptions in the model. We deal with each of these in turn.

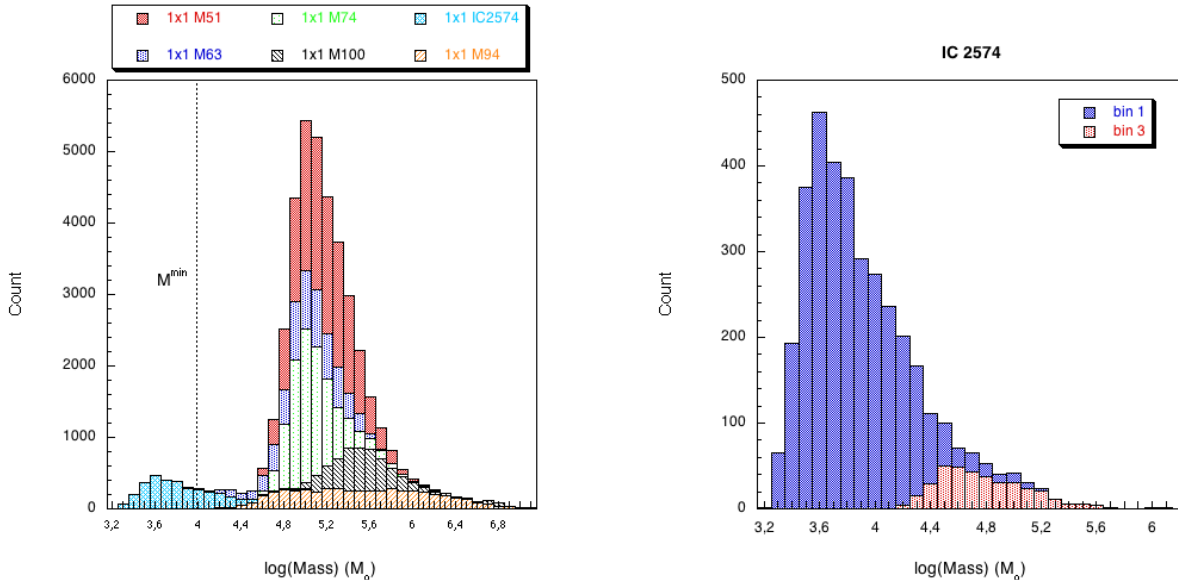


Figure 5. *Upper left:* The distribution of pixel stellar masses for all the galaxies of the sample, assuming the default 1×1 binning. The dotted line marks the limiting mass, M^{\min} , corresponding to the Lowest luminosity Limit of Cerviño et al. (2003). *Upper right:* The same for IC 2574 only in two instances of binning: 1×1 (blue shading) and 3×3 (red).

4.1 Lowest Threshold Pixel Mass for a Fully Sampled IMF

When stellar clusters are modeled by simple stellar population synthesis (SPS) techniques over a relatively small spatial extent, incomplete sampling of the initial mass function is a concern. Cerviño et al. (2003) have established a threshold called the Lowest Luminosity Limit (LLL), above which, synthesis models can be applied to stellar clusters to relate ionizing flux to newborn stellar mass. The mass of a stellar system with a completely sampled IMF and luminosity equal to the LLL is M^{\min} . The minimum mass depends on the metallicity, the age, the evolutionary tracks and model atmospheres used for the particular SPS model and Cerviño et al. (2003) publish these boundaries for SB99, as well as for their own models.

We have calculated the stellar masses of our pixels and compared with the values of M^{\min} given by Cerviño et al. (2003). Mass is calculated based on the FUV luminosity, as a more reliable estimator of the underlying stellar population. The pixel stellar mass is a lower limit derived by comparing the linearly scaled extinction-corrected observed L_{FUV} with the highest expected value from SB99, for a stellar population mass of $10^6 M_{\odot}$ at the youngest cluster ages. The M^{\min} for the SB99 models (with metallicities $Z = 0.02, 0.004$ and 0.008) is less than $10^4 M_{\odot}$ for the young stellar population, < 9 Myr, as it is in our case (cf. Cerviño et al. 2003, their Fig. 5).

Figure 5 shows the pixel mass distributions for each galaxy compared to the $10^4 M_{\odot}$ mass limit, using the 1×1 binning applied to all galaxies for our main results. Individual pixels range from ~ 10 to 50 pc on a side (Table 1). Save for the irregular IC 2574, all galaxies have pixel stellar masses greater than $10^4 M_{\odot}$, and therefore lie beyond the threshold for incomplete sampling of the IMF. IC 2574

is less massive than the rest of spiral galaxies of the sample, as it is usual for irregular galaxies. In the right panel of Fig. 5 we show the effect of binning the IC2574 data by 3×3 which puts the spatial sampling of IC 2574 above the threshold (cf. Fig. 5 of Cerviño et al. 2003). In the following section we show that the age map for IC 2574 is the same irrespective of whether 1×1 or 3×3 binning is used.

4.2 Spatial Binning Scale

We now examine the issue of whether the $H\alpha$ /FUV age calibration is valid on spatial scales other than those used for our results (1×1 binning). This is to verify whether the amount of $H\alpha$ and FUV flux in an individual pixel reflects the number of ionizing O and B stars within the same pixel. Our results should be independent of the geometry of individual HII regions on the scales at which we sample the galaxies.

Figure 6 shows coarser resampling of three galaxies (IC 2574, M94, and M51) using 3×3 and 6×6 binning, (to compare to the 1×1 binning used in Fig. 3). The three galaxies we have chosen are representative of the range of morphologies encountered in the full sample: spiral arms, a stellar ring, and a giant star forming complex. In the case of IC 2574, we concentrate on the giant northeastern star forming complex at the original sampling and 3×3 binning; the size of this star forming region is too small to justify the 6×6 .

As Fig. 6 shows, the age structures and gradients remain the same irrespective of binning scale used. This demonstrates the robustness of the pixel-based technique against systematics due to sampling. Furthermore, the resampling of the $24\mu\text{m}$ (1.5 arcsec), $70\mu\text{m}$ (4.5 arcsec) and $160\mu\text{m}$ (9 arcsec) *Spitzer* images to a common 1.5 arcsec plate scale

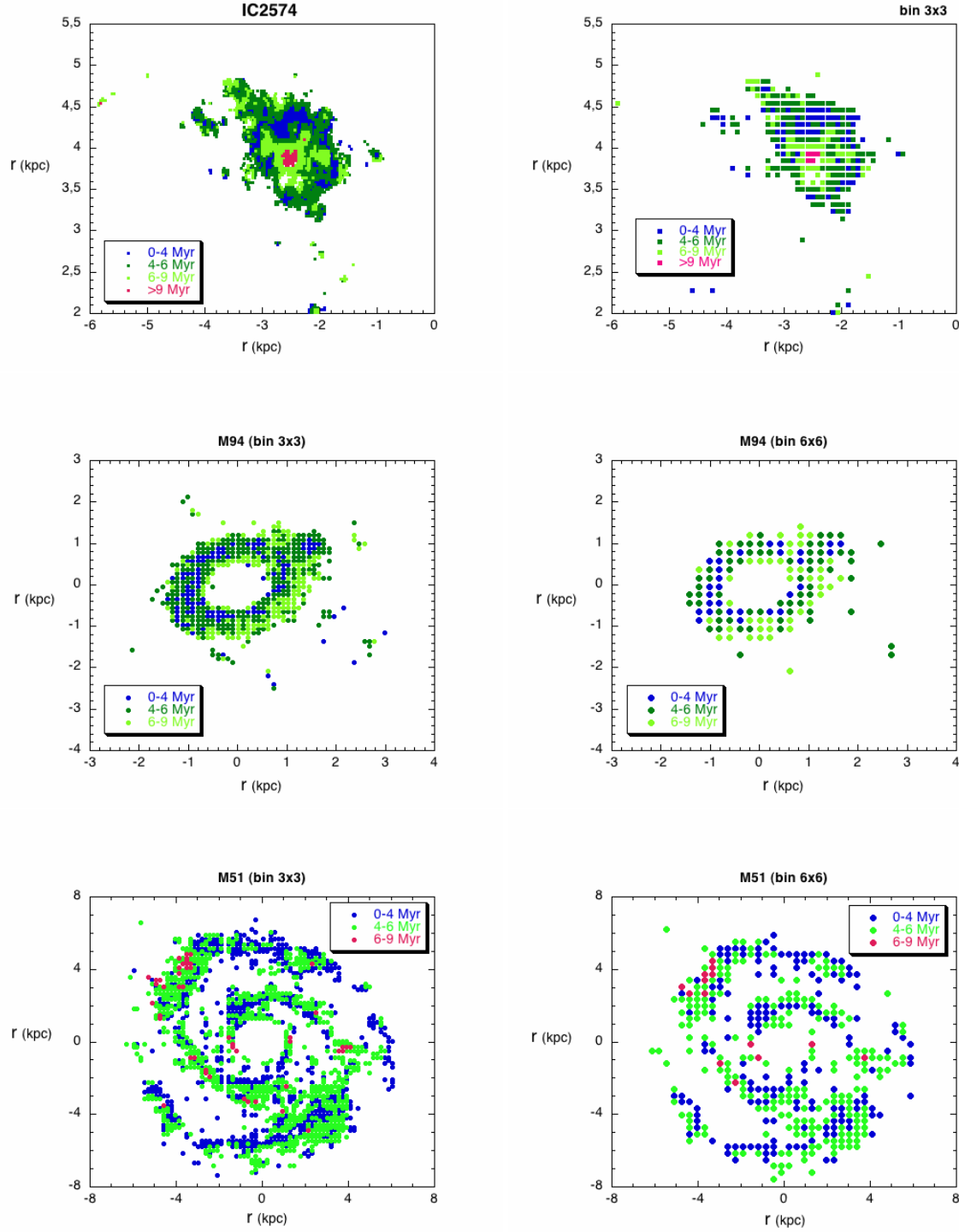


Figure 6. Age maps for IC2574, M94, and M51 derived by binning the data to coarser spatial scales. *upper panels:* A zoomed view of the northeastern stellar complex of IC 2574 at its original scale and with 3×3 binning. *middle panels:* M94 showing cases of 3×3 and 6×6 binning. *lower panels:* Same binning scales for M51. The pixel scales are $4.5''/\text{pix}$ and $9''/\text{pix}$ for 3×3 and 6×6 binning respectively.

has not affected our estimate of the total infrared flux nor its use in the dust corrections.

One of the galaxies in our test set, M51, has several independent flux measurements of its HII regions in the literature, against which we can test the robustness of our own measurements to the effects of binning. Scoville et al. (2001) show the distribution of HII diameters in M51 in their Fig. 13. Our smaller 1.5 arcsec pixel size corresponds to 70 pc (using the distance in Scoville et al), a size that encloses some 95% of all M51 HII regions. So even at the limit of our smallest sampling scale we have pixels that wholly contain the vast majority of HII regions in that galaxy.

4.3 Metallicity and IMF Variation

The ages we have derived depend on assumed values for metallicity, as well as the adopted initial mass function (IMF). We have calculated age maps from the full range of plausible metallicity and IMFs and used the spread in resulting ages to assign a measure of confidence to the age maps we have derived earlier. We also incorporate flux measurement uncertainties into the estimate. Each pixel age is computed for a grid of possible models spanning metallicity and IMF, and the mode of all ages, is chosen as the reference value. We define the confidence of our age estimation as the probability that the age stays with the same range (as set by the modal age) among all possible models. The confidence interval is calculated from the 3σ spread in computed ages from the modal age. Age values are binned in intervals of 0–4, 4–6, 6–9, and > 9 Myr, for the sake of clarity.

Fig. 8 shows the confidence and uncertainty maps for M74, as well as the lower pixel threshold mass (as calculated in Section 4.1). We also show the modal age map across all computed ages, which is a useful point of reference for our final mass maps presented in Sect. 3. Figures 8 – 12 show the same statistical estimates for the other galaxies in our sample. The average confidence across galaxies is 64–70%, with around 80% of pixels having confidence values in excess of 50%. The average uncertainty in age is 1.4 ± 0.5 Myr, well below the youngest ages (4 Myr) across all possible models. The youngest regions have the highest confidence values (in excess of $> 80\%$) and the lowest uncertainties. Examples of this are the inner ring in the stellar complex of IC 2574, the circumnuclear region of M94, or in the spiral arms of M100. Furthermore, comparing the mass maps with the confidence maps we do not find any effect of the mass in the age assignment. In M100 for example, there is a clear correspondence between the regions of high confidence with the most massive ones. But in M74 and M94 we find that there are regions of intermediate-high masses with lower confidence, probably due to a larger variability from the models.

5 DISCUSSION

This work shows that a comparison of the H α and FUV observations of nearby spiral galaxies is a relatively direct way to probe burst age variations in spirals. Age gradients are common features along or across the arms of grand-design spiral galaxies, as well as in circumnuclear (M94) and in irregular HII regions (IC 2574). In IC 2574, secondary star formation is observed on the periphery of the primary site

of star formation, and probably triggered by the latter. For M63, the age gradient occurs across the entire galactic disk, with the eastern side marked by a younger population (< 4 Myr), while in the inner ± 3 kpc of the western side an older population (6–9 Myr) dominates. Similarly in M74, there are age gradients across the spiral arms and an increasing age gradient from the inner to the outer parts of the galaxy. This corresponds with a very strong H α emission in the inner part of this galaxy.

The age maps presented here provide a global view of the star formation processes taking place in the galactic disks. They relate the maximum scale of coherent star formation to other large scale processes of star formation in galaxies, such as density waves and, in the case of M51, dynamics. However, it is beyond the scope of the present work to statistically favour one star formation mechanism over another given the extremely small sample size in hand.

One intriguing observational test recently proposed by Dobbs & Pringle (2010) predicts a different distribution of young star cluster ages depending on the mechanism for the excitation and maintenance of the spiral arms (see their Fig. 2). They suggest methods for age-dating clusters in nearby galaxies as a means of distinguishing between the various theoretical models for spiral arm formation. They consider four canonical galaxy models: (i) fixed pattern speed, (ii) galaxy with a bar, (iii) a flocculent spiral, and (iv) a tidally induced spiral. For each model in turn, they estimate the expected distribution of star clusters for ages ranging from ~ 2 to 130 Myr. Although our data only cover the most recent star formation episodes up to 10 Myr, we find a spatial distribution of regions consistent with the predictions of Dobbs & Pringle (2010), as well as a similar age distribution. M74, and to a lesser degree M100, show the expected distribution for a spiral with a fixed pattern speed and/or a bar, with a monotonic sequence of ages across the spiral arms from young to old, as predicted by standard density wave theory.

Our age maps for M74, M100 and M51 show the expected distribution for a spiral with a fixed pattern speed and/or a bar, with a monotonic sequence of ages across the spiral arms from youngest to oldest. Dobbs & Pringle (2010) model M51 as a tidally induced spiral undergoing a double interaction, and find that the age distribution of its star clusters (~ 2 Myr to 130 Myr) do not show the same trend as we have found in the younger age maps. Instead, their models show a rather a complex distribution, where clusters of different ages appear simultaneously in the same region. We infer that the youngest stellar populations show age gradients across the spiral arms, as predicted by standard spiral density wave theory.

In the cases of IC2574 and M94 it is difficult to identify a single possible mechanism for the triggering of star formation in these galaxies. The age map for IC 2574 only shows local regions, like the giant northeastern HII complex. Likewise for M94, the inner ring of intense active star formation dominates its age map. With observations of larger data sets the method developed here will be a powerful tool when applied to larger, statistically-significant samples of nearby star-forming galaxies.

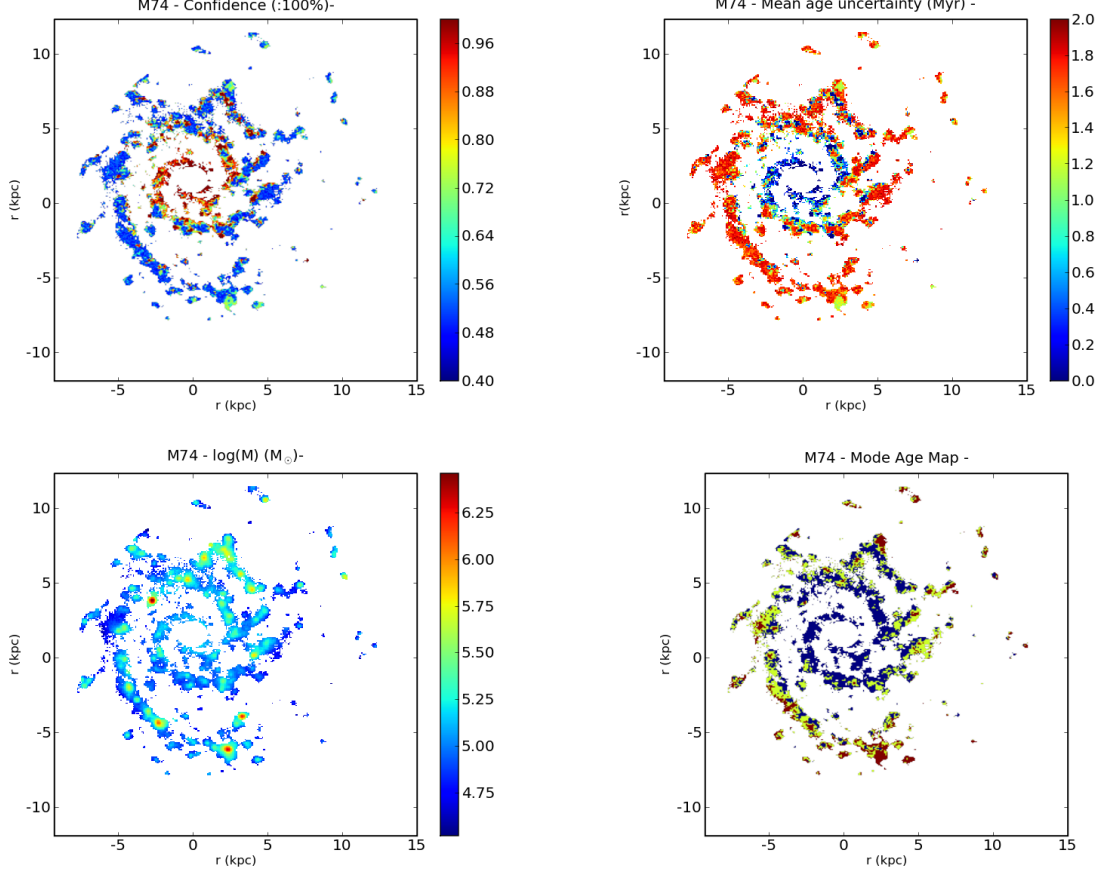


Figure 7. Statistical tests of the age map derived for the galaxy M74. *Upper left:* Confidence map of age assignments, expressed as a probability and calculated from the full range of plausible SB99 models. It also includes flux ratio uncertainties. *Upper right:* Map of age uncertainty, expressed in Myr. *Lower left:* Map of lower pixel threshold mass, calculated in Sect. 4.1. *Lower right:* Modal age map, in which each pixel age is the mode of all ages derived from the full range of plausible SB99 models and flux ratio uncertainties. The pixel scale is $1.5''/\text{pix}$

6 SUMMARY AND CONCLUSIONS

We have analyzed a sample of six spiral galaxies to study the recent history of their star formation. The study of the spatial distribution of recent and ongoing star formation provides key information about the evolutionary properties of gas-rich galaxies and the physical processes driving their evolution.

In this paper we have derived 2D age maps for each galaxy from a careful comparison of the UV and $\text{H}\alpha$ emission on a pixel-based basis, using Starburst 99 models to calibrate the relative fluxes in each band as function of age. While the absolute ages derived from this method may carry significant uncertainties, the *relative* ages derived through this technique are relatively reliable and robust. The use of a pixel-wise age dating technique allows age mapping of the youngest stellar population without prior assumptions about the spatial distribution of the star forming regions. The technique allows the spatial characterization of the age distribution which for HII regions within a range of distance in the Local Volume through their spatially-integrated light. The far infrared flux is used to correct for extinction due to dust on pixel-scales and the flux uncertainties in $F_{\text{H}\alpha}$ and F_{FUV} are folded in throughout.

Derivations of star formation ages in this way are subject to a number of systematic factors that we have carefully characterised to give confidence in our measurements. We have checked the validity of using a single stellar population model in pixel-sized regions by ensuring that our pixel-sized masses are well in excess of the minimum mass thresholds advocated by Cerviño et al. (2003). We have explored a range of different spatial binning scales to verify that undersampling does not affect the spatial distribution of ages. Finally, we have also run our models over a range of plausible IMFs and metallicities to yield confidence bounds on our derived ages. As a result of these tests, we have found that the average confidence in the age assignment is $64\text{--}70\%$, although in excess of 80% of regions have confidence values equal to or greater than this. We also find that the average combined uncertainty on our ages is 1.4 ± 0.5 Myr, much less than the youngest age bin (4 Myr) adopted for our analysis.

The age maps for our six galaxies exhibit a range of characteristics. The grand design spirals M74 and M100 show evidence of age gradients along the spiral arms, with youngest to oldest running from centre to edge. This is consistent with star formation induced by spiral wave density theory. With its nearby companion, NGC 5195, M51 is typi-

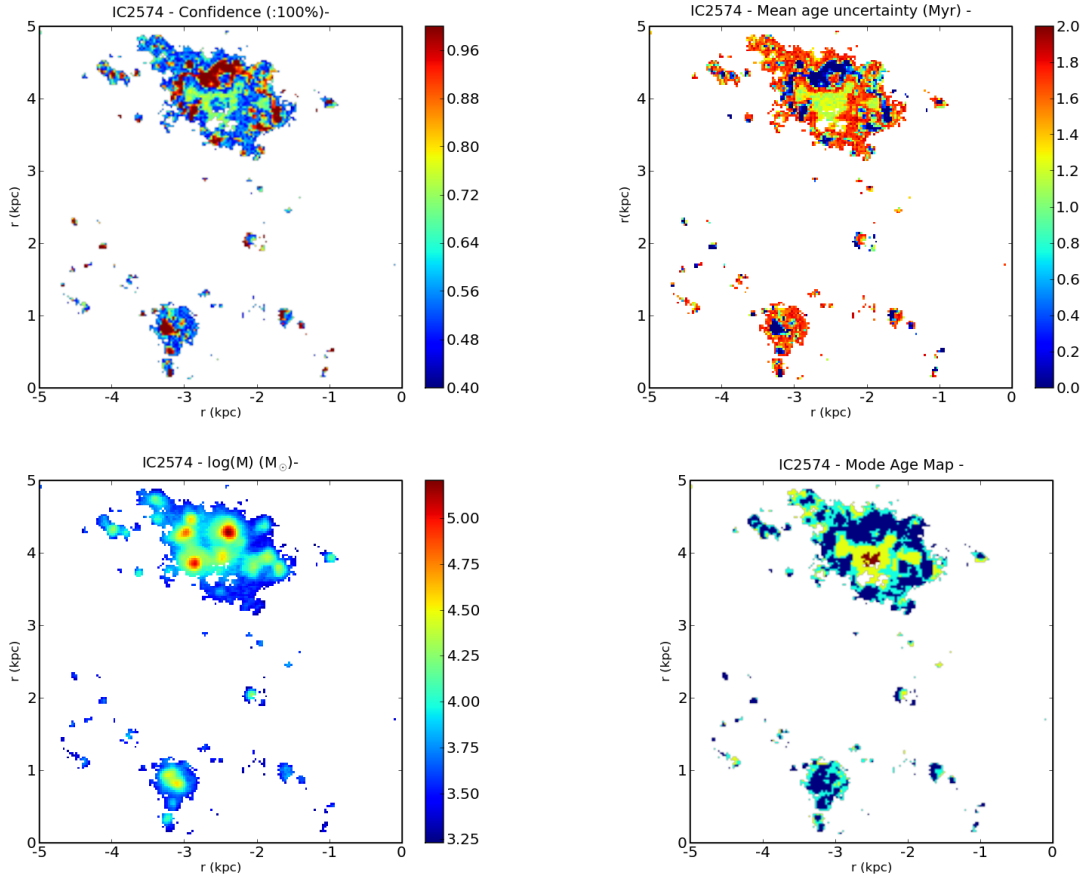


Figure 8. Same as Fig. 8 for the galaxy IC 2574.

cally modelled as a tidally induced spiral, undergoing a double interaction. However, its age distribution of star clusters, from ~ 2 Myr to around 130 Myr, does not show a clear trend with respect to its interacting companion and the most recent episodes of star formation. This lends support to the model of Salo & Laurikainen (1999) that sees NGC 5195 having already undergone multiple encounters with the disk of M51, with no preferred specific site for recent star formation. Multiple encounters are also needed to explain the long tidal tail of M51 to its companion and its characteristic kink. The flocculent spiral M63 shows a gradient from edge to edge rather than radially, suggesting that spiral density waves are not the dominant driver of star formation in such galaxies where the arms are more loosely wound and less well-defined.

ACKNOWLEDGMENTS

MCSG thanks the Anglo-Australian Observatory for hospitality during stays in 2007 and 2008 during which time the early stages of this work was completed. We also thank valuable input to this project from S. Ciani and M. Kildedar in its initial stages. This work is part of the PhD dissertation of M. Carmen Sánchez-Gil, funded by the Spanish Ministerio de Ciencia e Innovación (MICINN), under the FPU grant AP-2004-2196. We acknowledge financial sup-

port from Spanish MICINN through grants AYA2007-64052 and AYA2007-64712 and from Consejería de Educación y Ciencia (Junta de Andalucía) through TIC-101, TIC-4075 and TIC-114.

REFERENCES

- Abraham, R. G., Ellis, R. S., Fabian, A. C., Tanvir, N. R., & Glazebrook, K. 1999, MNRAS, 303, 641
- Akaike, H. 1974, IEEE Transactions on Automatic Control, 19, 716
- Allard, E. L., Knapen, J. H., Peletier, R. F., & Sarzi, M. 2006, MNRAS, 371, 1087
- Arsenault, R., Boulesteix, J., Georgelin, Y., & Roy, J.-R. 1988, A&A, 200, 29
- Battaglia, G., Fraternali, F., Oosterloo, T., & Sancisi, R. 2006, A&A, 447, 49
- Battinelli, P., Capuzzo-Dolcetta, R., Hodge, P. W., Vicari, A., & Wyder, T. K. 2000, A&A, 357, 437
- Bertin, E., & Arnouts, S. 1996, A&AS, 117, 393
- Bertin, G., & Lin, C. C. 1996, Spiral structure in galaxies a density wave theory, Publisher: Cambridge, MA MIT Press, 1996 Physical description x, 271 p. ISBN0262023962
- Bland-Hawthorn, J. 1995, IAU Colloq. 149: Tridimensional Optical Spectroscopic Methods in Astrophysics, 71, 72

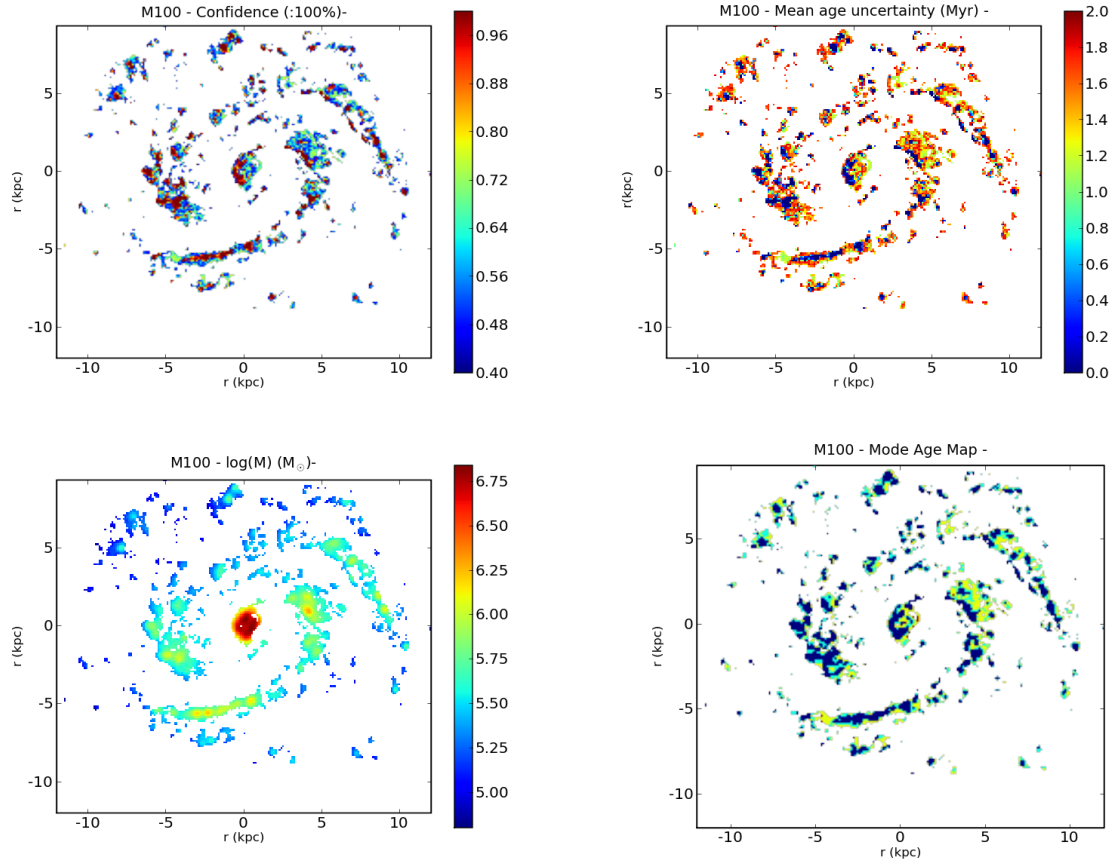


Figure 9. Same as Fig. 8 for the galaxy M100.

Bland-Hawthorn, J., & Jones, D. H. 1997, *The Hubble Space Telescope and the High Redshift Universe*, 121
 Boissier, S., et al. 2005, *ApJL*, 619, L83
 Boissier, S., et al. 2007, *ApJS*, 173, 524
 Bosma, A., van der Hulst, J. M., & Sullivan, W. T., III 1977, *A&A*, 57, 373
 Braun, R., Oosterloo, T. A., Morganti, R., Klein, U., & Beck, R. 2007, *A&A*, 461, 455
 Boomsma, R., Oosterloo, T. A., Fraternali, F., van der Hulst, J. M., & Sancisi, R. 2005, *Extra-Planar Gas*, 331, 247
 Bottema, R. 2003, *MNRAS*, 344, 358
 Buat, V., & Xu, C. 1996, *A&A*, 306, 61
 Buat, V., Donas, J., Milliard, B., & Xu, C. 1999, *A&A*, 352, 371
 Buat, V., et al. 2005, *ApJL*, 619, L51
 Calzetti, D., Kinney, A. L., & Storch-Bergmann, T. 1994, *ApJ*, 429, 582
 Calzetti, D. 1997, *American Institute of Physics Conference Series*, 408, 403
 Calzetti, D., et al. 2005, *ApJ*, 633, 871
 Cannon, J. M., et al. 2005, *ApJL*, 630, L37
 Cardelli, J. A., Clayton, G. C., & Mathis, J. S. 1989, *ApJ*, 345, 245
 Cepa, J., & Beckman, J. E. 1990, *ApJ*, 349, 497
 Cerviño, M., Luridiana, V., Pérez, E., Vílchez, J. M., & Valls-Gabaud, D. 2003, *A&A*, 407, 177

Chyży, K. T., & Buta, R. J. 2008, *ApJL*, 677, L17
 Ciani, S. 2003, *Anglo-Australian Observatory Epping Newsletter*, 102, 4
 Cid Fernandes, R., et al. 2004, *ApJ*, 605, 105
 Cid Fernandes, R., González Delgado, R. M., Storch-Bergmann, T., Martins, L. P., & Schmitt, H. 2005, *MNRAS*, 356, 270
 Cornett, R. H., et al. 1994, *ApJ*, 426, 553
 Cortese, L., et al. 2006, *ApJ*, 637, 242
 Dale, D. A., & Helou, G. 2002, *ApJ*, 576, 159
 Dale, D. A., et al. 2007, *ApJ*, 655, 863
 Dobbs, C. L., & Pringle, J. E. 2010, *MNRAS*, 1391
 Dubinski, J., Gauthier, J.-R., Widrow, L., & Nickerson, S. 2008, *Astronomical Society of the Pacific Conference Series*, 396, 321
 Dumke, A., Spiegel, M., Schmidt, R., & Neukum, G. 2008, *Lunar and Planetary Institute Science Conference Abstracts*, 39, 1910
 Efremov, Y. N. 2009, *Astronomy Letters*, 35, 507
 Elmegreen, D. M., & Elmegreen, B. G. 1987, *ApJ*, 314, 3
 Elmegreen, B. G., Elmegreen, D. M., & Montenegro, L. 1992, *ApJS*, 79, 37
 Eskridge, P. B., et al. 2003, *ApJ*, 586, 923
 Fathi, K., Beckman, J. E., Zurita, A., Relaño, M., Knapen, J. H., Daigle, O., Hernandez, O., & Carignan, C. 2007, *A&A*, 466, 905
 Feldmeier, J. J., Ciardullo, R., & Jacoby, G. H. 1997, *ApJ*,

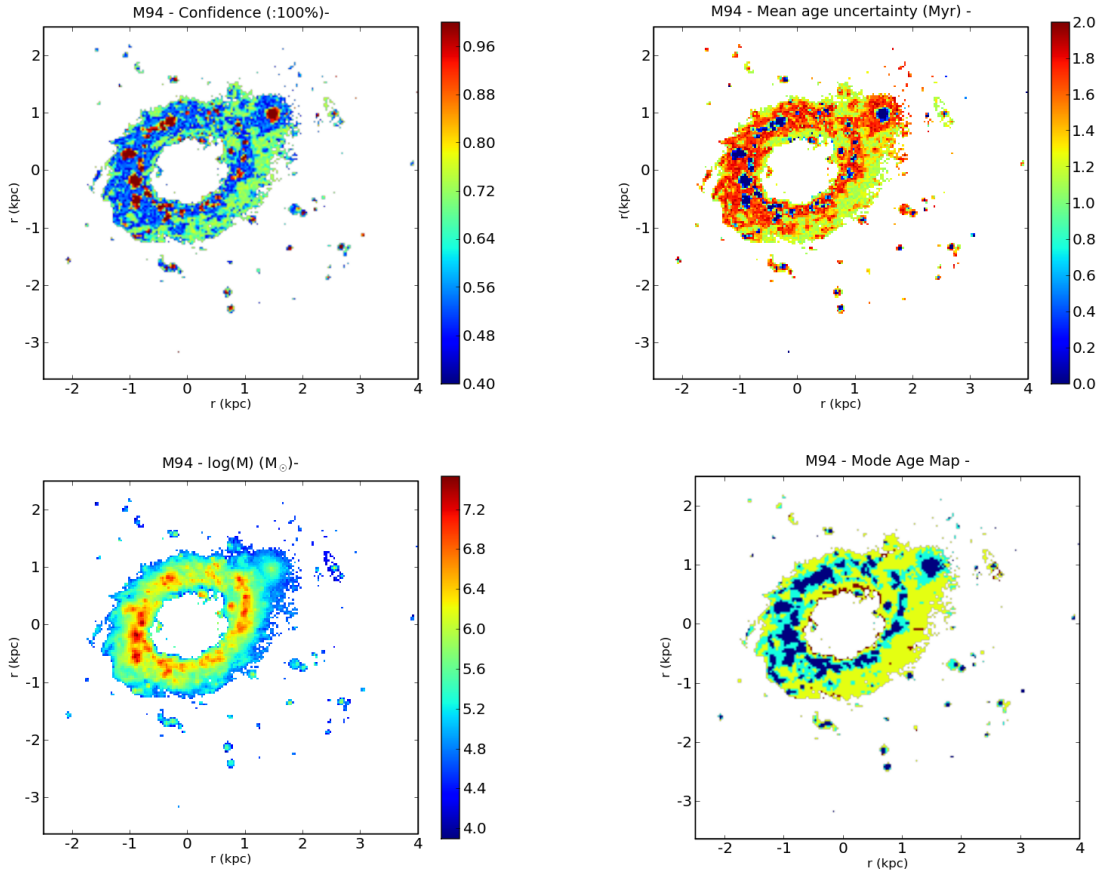


Figure 10. Same as Fig. 8 for the galaxy M94.

479, 231

Fraternali, F., Oosterloo, T. A., Sancisi, R., van Moorsel, G., & Cappi, M. 2002, *Seeing Through the Dust: The Detection of HI and the Exploration of the ISM in Galaxies*, 276, 419

Ganda, K., et al. 2007, *MNRAS*, 380, 506

Garcia-Burillo, S., Combes, F., & Gerin, M. 1993, *A&A*, 274, 148

Garcia-Burillo, S., Sempere, M. J., Combes, F., & Neri, R. 1998, *A&A*, 333, 864

Gerin, M., Casoli, F., & Combes, F. 1991, *A&A*, 251, 32

Glazebrook, K., Blake, C., Economou, F., Lilly, S., & Colless, M. 1999, *MNRAS*, 306, 843

González Delgado, R. M., Cid Fernandes, R., Pérez, E., Martins, L. P., Storchi-Bergmann, T., Schmitt, H., Heckman, T., & Leitherer, C. 2004, *ApJ*, 605, 127

Gordon, K. D., Clayton, G. C., Witt, A. N., & Misselt, K. A. 2000, *ApJ*, 533, 236

Grebel, E. K. 2000, *Star Formation from the Small to the Large Scale*, 445, 87

. Akaike, "A new look at the statistical model identification" *IEEE Transactions on Automatic and Control*, vol.19, pp. 716-723, 1974.

Heckman, T. M. 1980, *A&A*, 87, 152

Heckman, T., et al. 1995, *ApJ*, 452, 549

Ho, L. C., Filippenko, A. V., & Sargent, W. L. W. 1997, *ApJS*, 112, 315

Iglesias-Páramo, J., Boselli, A., Gavazzi, G., & Zaccardo, A. 2004, *A&A*, 421, 887

James, P. A., & Seigar, M. S. 1999, *A&A*, 350, 791

Jones, D. H., Shopbell, P. L., & Bland-Hawthorn, J. 2002, *MNRAS*, 329, 759

Kamphuis, J., & Briggs, F. 1992, *A&A*, 253, 335

Karachentsev, I. D., et al. 2002, *A&A*, 383, 125

Kennicutt, R. C., Jr. 1983, *ApJ*, 272, 54

Kennicutt, R. C., Jr. 1998, *ApJ*, 498, 541

Kennicutt, R. C., Jr., et al. 2003, *PASP*, 115, 928

Knapen, J. H., Shlosman, I., Heller, C. H., Rand, R. J., Beckman, J. E., & Rozas, M. 2000, *ApJ*, 528, 219

Knapen, J. H. 1998, *MNRAS*, 297, 255

Knapen, J. H., Beckman, J. E., Heller, C. H., Shlosman, I., & de Jong, R. S. 1995, *ApJ*, 454, 623

Knapen, J. H., Beckman, J. E., Shlosman, I., Peletier, R. F., Heller, C. H., & de Jong, R. S. 1995, *ApJL*, 443, L73

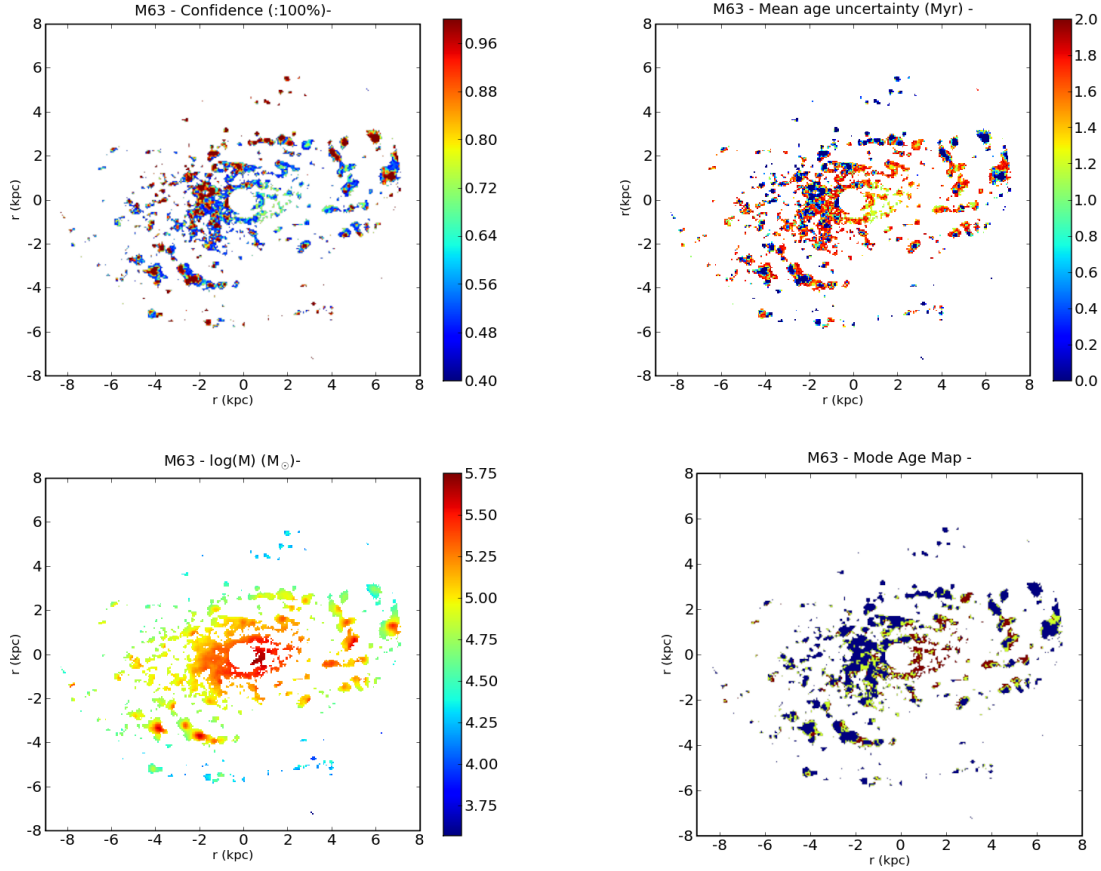
Knapen, J. H., Beckman, J. E., Cepa, J., van der Hulst, T., & Rand, R. J. 1992, *ApJL*, 385, L37

Knapik, J., Soida, M., Dettmar, R.-J., Beck, R., & Urbanik, M. 2000, *A&A*, 362, 910

Kong, X., Charlot, S., Brinchmann, J., & Fall, S. M. 2004, *MNRAS*, 349, 769

Kormendy, J., & Kennicutt, R. C., Jr. 2004, *ARA&A*, 42, 603

Kuno, N., Tosaki, T., Nakai, N., & Nishiyama, K. 1997,

**Figure 11.** Same as Fig. 8 for the galaxy M63.

PASJ, 49, 275

La Vigne, M. A., Vogel, S. N., & Ostriker, E. C. 2006, *ApJ*, 650, 818

Lanyon-Foster, M. M., Conselice, C. J., & Merrifield, M. R. 2007, *MNRAS*, 380, 571

Lee, J. C., et al. 2009, *ApJ*, 706, 599

Leitherer, C., et al. 1999, *ApJS*, 123, 3

Leitherer, C., Li, I.-H., Calzetti, D., & Heckman, T. M. 2002, *ApJS*, 140, 303

Lelièvre, M., & Roy, J.-R. 2000, *AJ*, 120, 1306

Lin, C. C., & Shu, F. H. 1964, *ApJ*, 140, 646

Luo, B., Chen, J.-Y., Zhang, Z.-L., Wang, Y., Wang, J.-Y., & Xu, H.-G. 2007, *Chinese Journal of Astronomy and Astrophysics*, 7, 335

Madau, P., Ferguson, H. C., Dickinson, M. E., Giavalisco, M., Steidel, C. C., & Fruchter, A. 1996, *MNRAS*, 283, 1388

Maoz, D., Filippenko, A. V., Ho, L. C., Rix, H.-W., Bahcall, J. N., Schneider, D. P., & Macchetto, F. D. 1995, *ApJ*, 440, 91

Martimbeau, N., Carignan, C., & Roy, J.-R. 1994, *AJ*, 107, 543

Martin, D. C., Fanson, J., Schiminovich, D., Morrissey, P., Friedman, P. G., Barlow, T. A., Conrow, T., Grange, R., et al., 2005, *ApJL*, 619, L1

Martin, M. C. 1998, *A&AS*, 131, 73

Martin, M. C. 1998, *VizieR Online Data Catalog*, 413, 10073

Martin, C. L., & Kennicutt, R. C., Jr. 2001, *ApJ*, 555, 301

Maoz, D., Koratkar, A., Shields, J. C., Ho, L. C., Filippenko, A. V., & Sternberg, A. 1998, *AJ*, 116, 55

Mazzuca, L. M., Knapen, J. H., Veilleux, S., & Regan, M. W. 2008, *ApJS*, 174, 337

Meurer, G. R., Heckman, T. M., & Calzetti, D. 1999, *ApJ*, 521, 64

Meurer, G. R., et al. 2009, *ApJ*, 695, 765

Miller, B. W., & Hodge, P. 1996, *ApJ*, 458, 467

Moellenhoff, C., Matthias, M., & Gerhard, O. E. 1995, *A&A*, 301, 359

Mulder, P. S., & van Driel, W. 1993, *A&A*, 272, 63

Mulder, P. S., & Combes, F. 1996, *A&A*, 313, 723

Natali, G., Pedichini, F., & Righini, M. 1992, *A&A*, 256, 79

Pasquali, A., et al. 2008, *ApJ*, 687, 1004

Paturel, G., Teerikorpi, P., Theureau, G., Fouqué, P., Musella, I., & Terry, J. N. 2002, *A&A*, 389, 19

Pei, Y. C. 1992, *ApJ*, 395, 130

Pellegrini, S., Fabbiano, G., Fiore, F., Trinchieri, G., & Antonelli, A. 2002, *A&A*, 383, 1

Pierce, M. J. 1986, *AJ*, 92, 285

Pilyugin, L. S., Vílchez, J. M., & Contini, T. 2004, *A&A*, 425, 849

Pogge, R. W. 1989, *ApJS*, 71, 433

Rozas, M., Zurita, A., Cardwell, A., & Beckman, J. E. 2000, *Cosmic Evolution and Galaxy Formation: Structure, Inter-*

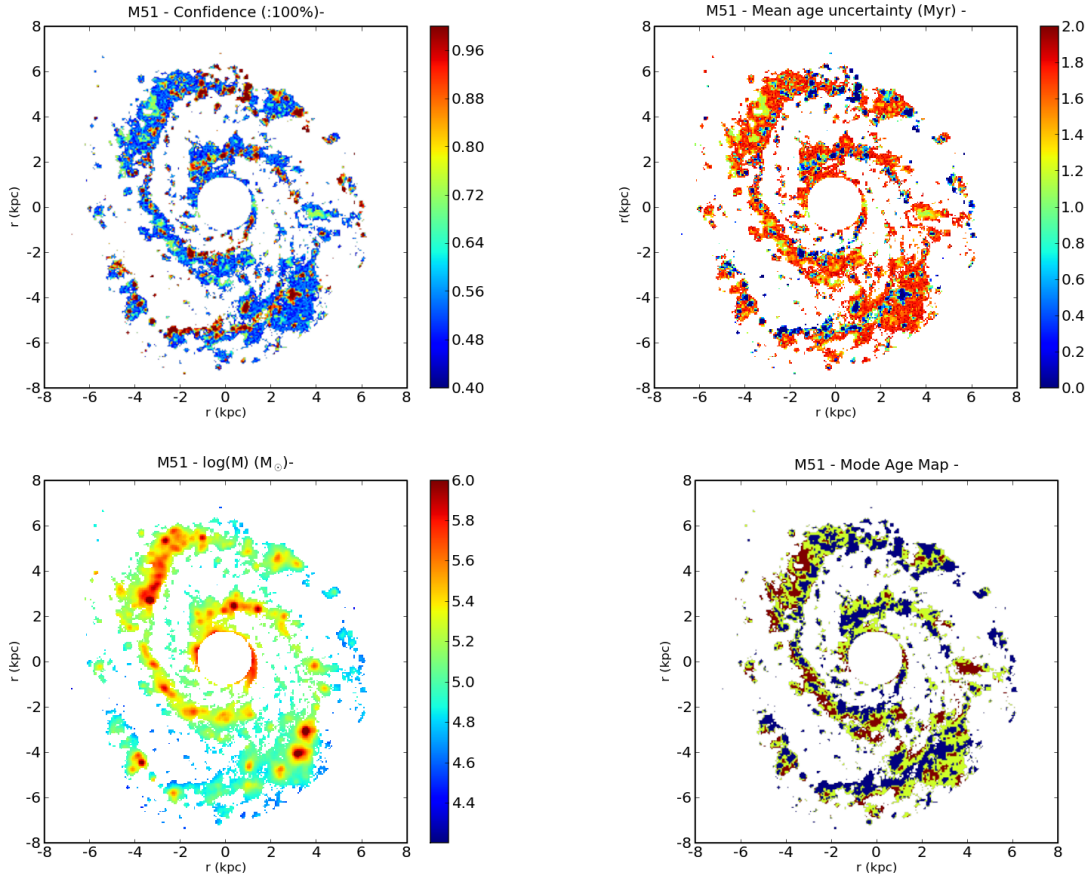


Figure 12. Same as Fig. 8 for the galaxy M51.

actions, and Feedback, 215, 230

Ryder, S. D., & Knapen, J. H. 1999, MNRAS, 302, L7

Ryder, S. D., Knapen, J. H., & Takamiya, M. 2001, MNRAS, 323, 663

Salo, H. & Laurikainen, E. 1999, Astrophysics & Space Science 269, 663

Sánchez Gil, M. C., Alfaro, E. J., & Pérez, E. 2009, ApJ, 702, 141

Sandage, A. 1961, Washington: Carnegie Institution, 1961, Scheepmaker, R. A., Lamers, H. J. G. L. M., Anders, P., & Larsen, S. S. 2009, A&A, 494, 81

Schlegel, D. J., Finkbeiner, D. P., & Davis, M. 1998, ApJ, 500, 525

Scoville, N. Z., Polletta, M., Ewald, S., Stolovy, S. R., Thompson, R., & Rieke, M. 2001, AJ, 122, 3017

Seigar, M. S. 2002, A&A, 393, 499

Sellwood, J. A., & Carlberg, R. G. 1984, ApJ, 282, 61

Shlosman, I., Frank, J., & Begelman, M. C. 1989, Nature, 338, 45

Sofue, Y., Tutui, Y., Honma, M., Tomita, A., Takamiya, T., Koda, J., & Takeda, Y. 1999, ApJ, 523, 136

Stecher, T. P., et al. 1992, ApJL, 395, L1

Stecher, T. P., et al. 1997, PASP, 109, 584

Swaters, R. A., Sancisi, R., & van der Hulst, J. M. 1997, ApJ, 491, 140

Thornley, M. D., & Mundy, L. G. 1997, ApJ, 484, 202

Tonry, J. L., Dressler, A., Blakeslee, J. P., Ajhar, E. A.,

Fletcher, A. B., Luppino, G. A., Metzger, M. R., & Moore, C. B. 2001, ApJ, 546, 681

Toomre, A. 1964, ApJ, 139, 1217

Trujillo, I., Martínez-Valpuesta, I., Martínez-Delgado, D., Peñarrubia, J., Gabany, R. J., & Pohlen, M. 2009, ApJ, 704, 618

Tosaki, T., Shioya, Y., Kuno, N., Nakanishi, K., & Hasegawa, T. 2003, PASJ, 55, 605

Tully, R. B. 1988, Cambridge and New York, Cambridge University Press, 1988, 221 p.,

Turner, J. L., & Ho, P. T. P. 1994, ApJ, 421, 122

Vázquez, G. A., & Leitherer, C. 2005, ApJ, 621, 695

Vogel, S. N., Rand, R. J., Gruendl, R. A., & Teuben, P. J. 1993, PASP, 105, 666

Wakker, B. P., & Adler, D. S. 1995, AJ, 109, 134

Waller, W. H., et al. 2001, AJ, 121, 1395

Walter, F., Kerp, J., Duric, N., Brinks, E., & Klein, U. 1998, ApJL, 502, L143

Walter, F., & Brinks, E. 1999, AJ, 118, 273

Weisz, D. R., Skillman, E. D., Cannon, J. M., Walter, F., Brinks, E., Ott, J., & Dolphin, A. E. 2009, ApJL, 691, L59

Wong, T., & Blitz, L. 2000, ApJ, 540, 771

Zimmer, P., Rand, R. J., & McGraw, J. T. 2004, ApJ, 607, 285 w

Zurita, A., Cardwell, A., Beckman, J. E., & Rozas, M. 2001, Galaxy Disks and Disk Galaxies, 230, 335

APPENDIX A: IRX- β RELATION

The IRX- β relation (Heckman et al. 1995, Meurer et al. 1999) relates the ultraviolet slope, β to the ratio of total infrared to UV flux, (defined as $IRX = F_{TIR}/F_{FUV}$). It demonstrates that the UV light absorbed by the dust is re-emitted as thermal emission in the far infrared, thereby allowing one to estimate the extinction in the UV from the slope. Here we independently derive our own IRX- β relation based on our pixel-based analysis of the six star forming galaxies in our sample.

Values of the UV spectral slope were derived per pixel for each of the six galaxies according to the definition of Kong et al. (2004),

$$\beta = \frac{\log(f_{FUV}) - \log(f_{NUV})}{\log(\lambda_{FUV}) - \log(\lambda_{NUV})} \quad (A1)$$

where f_{FUV} and f_{NUV} are the far- and near-UV fluxes from the respective FUV and NUV GALEX filters (in $\text{ergs}^{-1}\text{cm}^{-2}\text{\AA}^{-1}$). The central wavelengths of each bandpass are $\lambda_{FUV} = 1520 \text{\AA}$, $\lambda_{NUV} = 2310 \text{\AA}$. The total far-infrared fluxes were calculated as described in Sect 2.

Cortese et al. (2006) use a linear fit between the $\log(IRX)$ and β ,

$$\log(IRX) = a + b\beta \quad (A2)$$

although other authors (Kong et al. 2004, Boissier et al. 2007) have found that adding a non-linear term

$$IRX = 10^{a+b\beta} - c \quad (A3)$$

produces a better fit to the data. We have fitted both linear and non-linear relations to our $\log(IRX)$ - β relation and compared our results to these authors. Outliers were rejected if they were beyond 4-standard deviations of the mean. The linear fit was calculated using a classical ordinary least squares fit (OLS) of $\log(IRX)$ on β and vice versa. The final fit was taken as the bisector of the two OLS lines and is the fit is similar to that given by Cortese et al. (2006) for an optically-selected sample of normal star-forming galaxies in nearby clusters. The upper left panel of Fig. A1 shows our fits to the full sample compared to those of Cortese et al. (2006) and the fit parameters are summarised in Table A1.

The upper right panel of Fig. A1 shows our non-linear fit to the same data compared to those of Kong et al. (2004) and Boissier et al. (2007). Our fit is closer to that of Kong et al. but shifted to higher values of β and with smaller slope, Kong et al. use a sample of 50 starburst galaxies, while Boissier et al. take a sample of 43 nearby, late-type galaxies. With the exception of the interacting M51, it can be argued that all the galaxies in our sample are normal quiescent star forming systems. However, because we consider emission on pixel scales (rather than on a galaxy-wide scale), each pixel ought to be considered as a HII region, in which case we would expect the behaviour to be closer to the starburst sample fitted by Kong et al., as is seen in Fig. A1. Table A1 gives the parameters of each non-linear fit.

We use the Akaike Information Criterion (AIC; Akaike 1974) to choose the better fit between the linear and non-linear cases, defined as

$$AIC = -2\ln(L) + 2K \quad (A4)$$

where $\ln(L)$ is the logarithm of maximized likelihood function, and K is the number of parameters in the model. In the case of least squares regression for normally distributed errors, (as it is the case here), it can be computed as

$$AIC = N\log(\hat{\sigma}^2) + 2K \quad (A5)$$

where $\hat{\sigma}^2$ is the variance and N is the sample size. The ‘best’ model is that with the lowest AIC among a set of specified models, and which best describes the data with the fewest number of free parameters. Applying equation (A5) to the fits from equations (A2) and (A3) reveal the non-linear relation to be the better fit of the two.

The pixel points in the upper left panel of Fig. A1 are colour-coded by galaxy and highlight the different regions occupied by each galaxy in the IRX- β plane. The points of the irregular galaxy IC 2574 are confined to lower IRX and β values in contrast with the other spiral galaxies. We note that M51 exhibits the greatest scatter about its IRX- β fit compared to the other spirals.

The lower panels of Fig. A1 show the curves of best fit for each galaxy compared to the overall fit for the sample, in both the linear (left panel) and non-linear (right panel) cases. While the non-linear case is a better fit to the sample as a whole, it would appear to be inappropriate in the case of individual galaxies. Notwithstanding our small sample size, the upper left panel of Fig. A1 suggest that different morphologies are reflected in varying ranges for IRX and β , and would explain the non-linear nature of the full sample. We would conclude that for a sufficiently restricted mix of morphological types and galaxy mass, the IRX- β relation is linear, and that care should be exercised when fitting a sample that is not.

Table A2 lists the fit parameters to individual galaxies for both the linear and non-linear case.

This paper has been typeset from a \TeX / \LaTeX file prepared by the author.

Table A1. IRX- β fits for the full sample

Fit	This paper		Literature
Linear	OLS(Y X)	$\log(\text{IRX}) = 0.459(\pm 0.002)\beta + 1.001(\pm 0.002)$, $R = 0.662$	$\log(\text{IRX}) = 0.7(\pm 0.06)\beta + 1.30(\pm 0.06)^{(a)}$
	OLS(X Y)	$\beta = 1.033(\pm 0.006)\log(\text{IRX}) - 1.387(\pm 0.005)$, $R = 0.662$	
	OLS bisector	$\log(\text{IRX}) = 0.662(\pm 0.004)\beta + 1.151(\pm 0.004)$	
Non-linear	$\text{IRX} = 10^{1.225(\pm 0.009) + 0.239(\pm 0.004)\beta - 3.736(\pm 0.311)}$, $R = 0.589$		$\text{IRX} = 10^{2.10 + 0.85\beta} - 0.95^{(b)}$
			$\text{IRX} = 10^{1.145 + 0.324\beta} - 3.136^{(c)}$

^(a)Cortese et al. 2006^(b)Kong et al. 2004^(c)Adapted from Boissier et al. 2007; The fit given is $\text{IRX} = 10^{0.561 + 0.713(\text{FUV} - \text{NUV})} - 3.136$, where FUV-NUV is the color between the two GALEX bands. The direct relation between β and the (FUV-NUV) is given by equation A1.**Table A2.** IRX- β fits by galaxy

	Linear fit: $\log(\text{IRX}) = \tilde{a}\beta + \tilde{b}$			Non-linear fit: $\text{IRX} = 10^{a+b\beta} - c$				R
	\tilde{a}	\tilde{b}	R	a	b	c		
M51	0.575 \pm 0.007	1.155 \pm 0.010	0.493	1.292 \pm 0.031	0.169 \pm 0.013	6.245 \pm 1.36		0.412
M63	0.409 \pm 0.008	1.191 \pm 0.009	0.659	1.107 \pm 0.027	0.288 \pm 0.014	-3.687 \pm 0.72		0.639
M74	0.623 \pm 0.015	1.090 \pm 0.014	0.357	0.631 \pm 0.078	0.223 \pm 0.054	-1.739 \pm 0.75		0.276
M94	0.564 \pm 0.009	1.156 \pm 0.011	0.673	1.241 \pm 0.033	0.185 \pm 0.016	5.79 \pm 1.28		0.672
M100	0.590 \pm 0.011	1.070 \pm 0.001	0.674	1.099 \pm 0.023	0.305 \pm 0.014	1.518 \pm 0.59		0.693
IC 2574	0.835 \pm 0.016	1.042 \pm 0.043	0.44	0.231 \pm 0.026	0.245 \pm 0.054	0.112 \pm 0.16		0.359

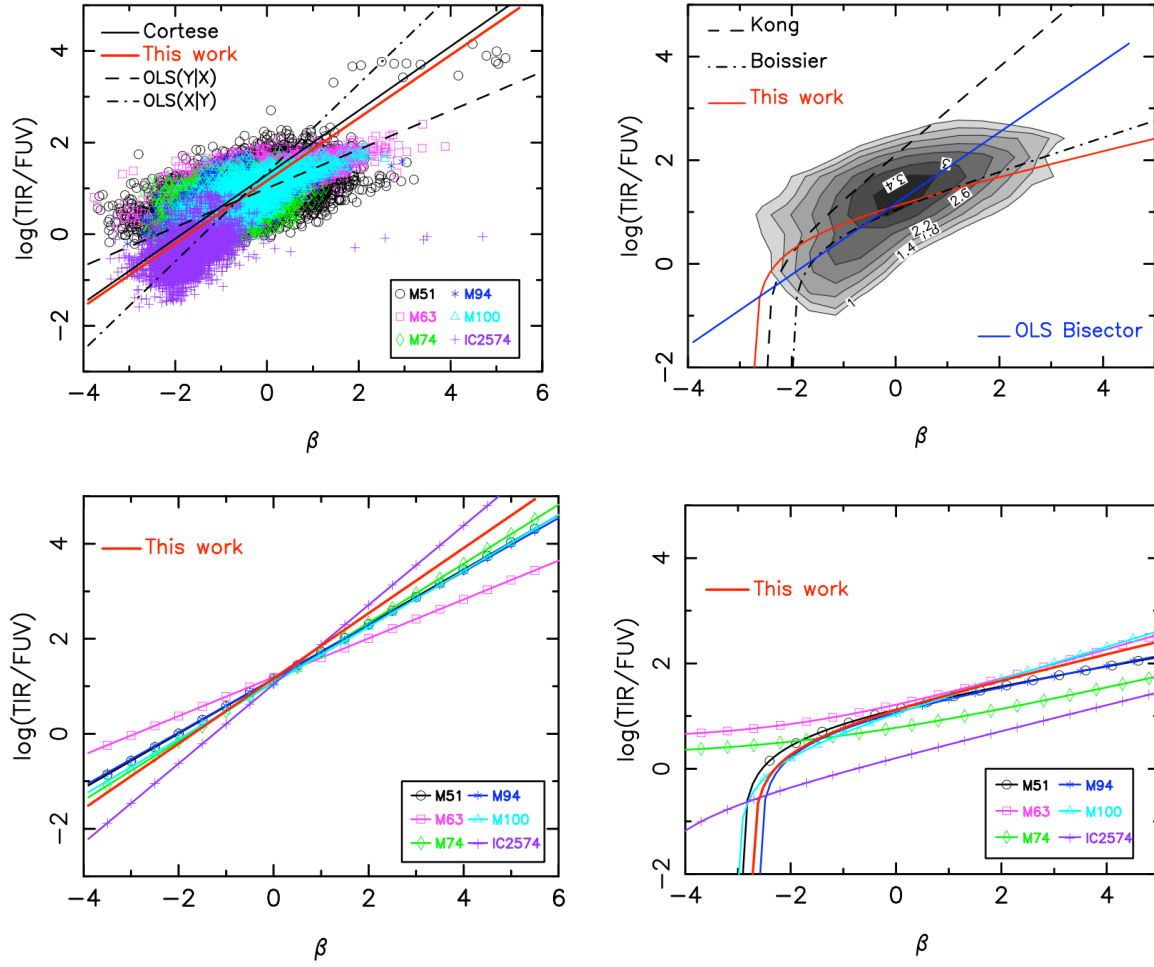


Figure A1. IRX- β plots where each galaxy is represented by a different colour and symbol, as specified in the key. *upper left:* Linear fit for all points combined (red line) compared to that of Cortese et al. (2006) (black line). Also shown are the OLS (Ordinary Least Squares) bisectors OLS(Y|X) and OLS(X|Y) from which our full fit was derived. *upper right:* Non-linear fit for all points combined (red line) compared to those of Kong et al. (2004) (dashed line) and Boissier et al. (2007) (dot-dash line). In this case we have plotted our full sample as a density distribution with log contours. Also shown (blue line) is the linear fit from the upper left panel. *lower left:* Linear fits of the IRX- β relation for individual galaxies, using identical colours and symbols to those in the upper left panel. *lower right:* Non-linear fits per galaxy showing the same colours and symbols as the other panels.